Durham University

Durham Research Online

Deposited in DRO:

08 August 2014

Version of attached file:

Published Version

Peer-review status of attached file:

Peer-reviewed

Citation for published item:

Lira, P. and Ward, M. and Zezas, ,A. and Alonso-Herrero, A. and Ueno, S. (2002) 'Chandra observations of the luminous infrared galaxy NGC 3256.', Monthly notices of the Royal Astronomical Society., 330 (2). pp. 259-278.

Further information on publisher's website:

http://dx.doi.org/10.1046/j.1365-8711.2002.05014.x

Publisher's copyright statement:

This article has been accepted for publication in Monthly notices of the Royal Astronomical Society © 2002 The Authors Published on behalf of Royal Astronomical Society. All rights reserved.

Additional information:

Use policy

The full-text may be used and/or reproduced, and given to third parties in any format or medium, without prior permission or charge, for personal research or study, educational, or not-for-profit purposes provided that:

- a full bibliographic reference is made to the original source
- a link is made to the metadata record in DRO
- the full-text is not changed in any way

The full-text must not be sold in any format or medium without the formal permission of the copyright holders.

Please consult the full DRO policy for further details.

Durham University Library, Stockton Road, Durham DH1 3LY, United Kingdom
Tel : +44 (0)191 334 3042 | Fax : +44 (0)191 334 2971
https://dro.dur.ac.uk

Mon. Not. R. Astron. Soc. **330,** 259–278 (2002)

Chandra observations of the luminous infrared galaxy NGC 3256

P. Lira,[1,2]★ M. Ward,[1] A. Zezas,[3] A. Alonso-Herrero[4,5] and S. Ueno[6]

[1]*Department of Physics & Astronomy, University of Leicester, Leicester LE1 7RH*
[2]*Departamento de Astronomía, Universidad de Chile, Casilla 36-D, Santiago, Chile*
[3]*Harvard–Smithsonian Center for Astrophysics, 60 Garden Street, Cambridge MA 02138, USA*
[4]*Department of Physical Science, University of Hertfordshire, Hatfield, Herts AL10 9AB*
[5]*Steward Observatory, University of Arizona, Tucson, AZ 85721, USA*
[6]*Space Utilization Research Program, National Space Development Agency of Japan (NASDA), Tsukuba Space Center, 2-1-1 Sengen, Tsukuba, Ibaraki 305, Japan*

Accepted 2001 October 5. Received 2001 October 5; in original form 2001 February 16

Downloaded from http://mnras.oxfordjournals.org/ at University of Durham on August 8, 2014

ABSTRACT

We present a detailed analysis of high-resolution *Chandra* observations of the merger system NGC 3256, the most infrared-luminous galaxy in the nearby universe. The X-ray data show that several discrete sources embedded in complex diffuse emission contribute $\gtrsim 20$ per cent of the total emission ($L_{\rm X}^{\rm tot} \sim 8 \times 10^{41}$ erg s^{-1} in the 0.5–10 keV energy range). The compact sources are hard and extremely bright and their emission is probably dominated by accretion-driven processes. Both galaxy nuclei are detected with $L_{\rm X} \sim 3\text{–}10 \times 10^{40}$ erg s^{-1}. No evidence is found for the presence of an active nucleus in the southern nucleus, contrary to previous speculation. Once the discrete sources are removed, the diffuse component has a soft spectrum that can be modelled by the superposition of three thermal plasma components with temperatures $kT = 0.6$, 0.9 and 3.9 keV. Alternatively, the latter component can be described as a power law with index $\Gamma \sim 3$. Some evidence is found for a radial gradient of the amount of absorption and temperature of the diffuse component. We compare the X-ray emission with optical, Hα and *NICMOS* images of NGC 3256 and find a good correlation between the inferred optical/near-infrared and X-ray extinctions. Although inverse Compton scattering could be important in explaining the hard X-rays seen in the compact sources associated with the nuclei, the observed diffuse emission is probably of thermal origin. The observed X-ray characteristics support a scenario in which the powerful X-ray emission is driven solely by the current episode of star formation.

Key words: galaxies: active – galaxies: general – galaxies: individual: NGC 3256 – galaxies: nuclei – X-rays: galaxies.

1 INTRODUCTION

The *IRAS* all-sky survey revealed a class of galaxies with infrared luminosities that overlap the bolometric luminosity of quasars. The vast amounts of energy released by these luminous infrared galaxies (LIRGs: $L_{\rm IR} > 10^{11}\,{\rm L}_\odot$) and ultraluminous infrared galaxies (ULIRGs: $L_{\rm IR} > 10^{12}\,{\rm L}_\odot$) opened a question that has still not been completely resolved: what is the primary source of their power? The two favoured answers are extreme starburst activity or the presence of an active nucleus. Important clues came from the observed correlation between infrared luminosity and the presence of an AGN, showing that the fraction of Seyfert nuclei detected in optical surveys increases from ~5 per cent to ~50 per cent for objects with $\log L_{\rm IR} \sim 10.5\,{\rm L}_\odot$ and $\log L_{\rm IR} \sim 12.5\,{\rm L}_\odot$, respectively (Sanders & Mirabel 1996).

The definite presence (or absence) of an AGN in infrared-luminous systems is difficult to test, since tens or even hundreds of magnitudes of visual extinction are routinely derived for the central regions of these galaxies. However, recent results from mid-infrared observations using *ISO*, which can probe regions with extinctions as high as $A_V \sim 50$ mag, show that 70–80 per cent of ULIRGs are predominantly powered by star-formation activity (Genzel et al. 1998; Lutz, Veilleux & Genzel 1999).

Since nearly all ULIRGs have distorted morphologies, it has been suggested that galactic interactions displace large masses of molecular gas into the central few kpc of these systems, fuelling a powerful starburst or an accretion-powered AGN. Several possible evolutionary scenarios have been proposed to link ULIRGs with QSOs, 'super-starbursts' and elliptical galaxies (Sanders et al. 1988; Joseph & Wright 1985; see also Lípari et al. 2001 and references therein).

NGC 3256 is a spectacular merger system. Its infrared luminosity of $6 \times 10^{11}\,{\rm L}_\odot$ makes it the most luminous object in

★E-mail: plt@star.le.ac.uk

© 2002 RAS

the local ($z < 0.01$) universe.[1] Evidence of a recent interaction is the presence of 200 kpc extended tails and a highly chaotic nuclear region (Graham et al. 1984). Direct evidence for the presence of a powerful starburst in the galaxy comes from the detection of strong absorption features from massive stars (Doyon, Joseph & Wright 1994; Lípari et al. 2000). The central region of the starburst (~ 5 kpc across) is characterized by strong near-infrared line emission, high metallicities and outflows (Moorwood & Oliva 1994; Lípari et al. 2000). A double nucleus has been detected at radio and near-infrared frequencies (Norris & Forbes 1995; Kotilainen et al. 1996), suggesting that NGC 3256 is not a very advanced merger system. While the northern nucleus has always been recognized as a pure starburst, the presence of a hidden AGN in the southern nucleus has remained a matter of speculation.

X-ray observations of NGC 3256 were obtained previously with *ROSAT* and *ASCA*. From the analysis of *ASCA* data, Moran, Lehnert & Helfand (1999, hereafter MLH) determined a total luminosity in the 0.5–10 keV energy range of 1.6×10^{42} erg s^{-1}. If powered solely by star formation, NGC 3256 would represent the top end of the X-ray luminosity distribution of starburst galaxies. MLH also argued that the observed power-law tail could not be explained by the presence of an AGN or a population of Galactic-type X-ray binaries and suggested that inverse Compton scattering could provide a substantial fraction of the observed high-energy component.

In order to understand the nature of the NGC 3256 powerful emission, observations at high spatial resolution are required. High-resolution X-ray observations are particularly suited for this aim, since hard X-rays are able to probe deep into the most obscured regions and give vital information about hot gaseous components commonly associated with strong starbursts and undetectable at other wavelengths. In this paper we report recent high resolution observations of NGC 3256 made using the *Chandra* X-ray Observatory. This paper is organized as follows: Section 2 gives details of the data analysis procedure, while Sections 3 and 4 focus on the characteristics of the population of compact sources and the diffuse emission, respectively; in Section 5 a brief comparison between the *Chandra* and *ASCA* observations is given; a full discussion is presented in Section 6 and conclusions and a summary can be found in Section 7.

2 OBSERVATIONS AND DATA ANALYSIS

A *Chandra* 28-ks observation of NGC 3256 was obtained on 2000 January 5. For an assumed distance of 56 Mpc, 1 arcsec – encircling ~ 90 per cent of the photons at 1.5 keV from a point source[2] – corresponds to a linear size of 270 pc. The data were analysed using a combination of *Chandra* X-ray Center (CXC) CIAO (v1) and HERSARC XSPEC (v10.0) software. The galaxy was imaged using the (back-illuminated) ACIS S3 chip, which is known to suffer from flares of high background radiation. An examination of our observations, after discarding all events outside the 0.3–10.0 keV energy range, showed that in fact about half of the observing time was affected by high background. The strategy adopted to ensure minimum contamination from the high background episodes is described in Sections 3 and 4.1. The average count rate during the observation was found to be 2.55 counts per second in the S3 chip, compared with the quiescent 0.79 counts per second measured in-flight.[2] The three known bad columns of the S3 chip were located far away (~ 5 arcmin) from our target and therefore did not induce any problems during the data analysis.

Simple aperture photometry shows that all the galactic emission is contained within a circle of radius ~ 60 arcsec, while circles of radius ~ 27 and ~ 18 arcsec encircle ~ 95 per cent and ~ 90 per cent of the counts, respectively. The large first radius is necessary to contain the two most distant discrete sources (sources 1 and 14 in Fig. 1 and Table 1), which are located at ~ 40–55 arcsec from the central peak of emission.

Owing to a calibration error in early *Chandra* data, the astrometry of the original observations of NGC 3256 were affected by an ~ 8-arcsec shift in absolute astrometry. After reprocessing of the data at the CXC, which corrected for this problem, we found that the position of the brightest X-ray compact source seen in the galaxy (source 7 in Fig. 1 and Table 1) was offset with respect to the radio position for the northern nucleus (which is coincident, within 1 arcsec, with the position of the nucleus seen at optical and infrared wavelengths – Norris & Forbes 1995) by only 0.44 arcsec. Also, good positional agreement is found between several knots of emission seen in X-rays and optical wavelengths (see Sections 6.2 and 6.3.1).

Fig. 1 shows a $\sim 60 \times 60$ arcsec *Chandra* image of NGC 3256 in the 0.3–1.5 and 1.5–10 keV energy ranges. The soft image shows a significant and spatially-complex diffuse component. Several of the discrete sources are more easily seen in the harder band, where the diffuse emission has a much lower surface brightness. The emission is dominated by a strong compact source located at the centre of the X-ray-emitting region and labelled as source 7. As mentioned above, this source has been identified with the northern nucleus of the galaxy. Another, harder source is found 5 arcsec to the south of this position in the 1.5–10 keV band (source 8), and is identified as the X-ray counterpart of the southern nucleus. The diffuse emission shows complex morphology, with a strong central 'Bar' running in an ES to NW direction just above of the northern nucleus. Another interesting feature is a southern 'Arm' connecting sources 8 and 2, which leaves a void of soft X-ray emission at the position of the southern nucleus.

3 DISCRETE SOURCES

A wavelet detection algorithm was used to search for compact sources associated with NGC 3256. This algorithm is particularly suited for the detection of closely-spaced and extended sources. However, given the strong and complex extended-emission component in the central region of NGC 3256, it is still possible that strong fluctuations of the background can be identified as spurious sources. For this reason, the detection algorithm was run using an image in the 1.5–10 keV energy range only, where discrete sources are more conspicuous. Also, low surface brightness and obviously extended sources in the Arm and to the NW of the bright central source were disregarded since their morphology did not appear less smeared in the hard-band image. The final source list was compiled only after the determination of the detection significance for each source. A total of 14 compact sources were found with a detection significance, i.e. (source counts)/(background standard deviation), ranging from ~ 140 to ~ 12 (see Table 1). The sources are shown in Fig. 1 and labelled from 1 to 14 with increasing right ascension.

For each discrete source a background-subtracted number of

[1] A distance of 56 Mpc ($z = 0.009$, $H_\circ = 50$ km s^{-1} Mpc^{-1}) has been used throughout this paper.

[2] See the *Chandra* Proposers' Observatory Guide v3.0, 2000 December. http://asc.harvard.edu/udocs/docs/POG/MPOG/

Downloaded from http://mnras.oxfordjournals.org/ at University of Durham on August 8, 2014

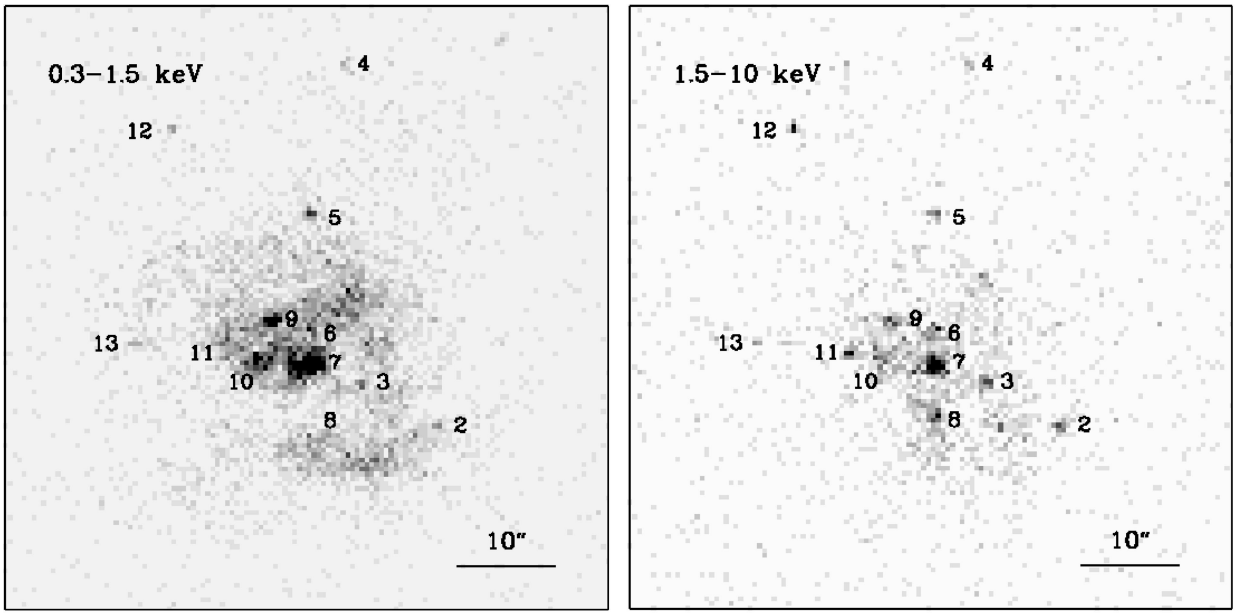

Figure 1. *Chandra* images of NGC 3256 in the 0.3–1.5 keV (left) and 1.5–10 keV (right) energy ranges. The images extend ∼60 arcsecs on each side. North is at the top and East is on the left. Discrete sources are labelled by increasing order of right ascension. Sources 1 and 14 are not included in the figure (see Table 1 for celestial coordinates).

counts was obtained from within an $r = 3.5$ pixel ap/erture (1.72 arcsec). This encircles ∼ 99 per cent of the photons at 0.3 keV and ∼ 90 per cent of the photons at 5.0 keV (in general, sources were not detected above this energy). The small apertures used imply that on average only ∼ 2 of the source counts are expected to correspond to the background. Therefore, the study of these sources was done without screening out the high background episodes. None of the sources was affected by pileup. For each individual source, a local background region was defined by using an annulus with $r \sim 5$–10 pixels centred at the position of the source with holes excised at the positions of any other nearby compact sources. The determined counts and associated significance can be found in Table 1.

3.1 Spatial analysis

We have analysed the spatial profile of the detected sources. To do this we obtained locally background-subtracted counts within circular apertures of radius 1, 2, 3, 4 and 5 pixels and compared them with model PSFs generated at the position of each source (Fig. 2). The full 0.3–10 keV band image was used to obtain the source profiles, except for both nuclei, for which a harder 2–5 keV band image was used. In this way the amount of diffuse emission around the northern nucleus was minimized, and the detectability of the obscured southern nucleus was maximized. The major difficulties in obtaining a meaningful analysis of the profiles are the poor sampling of the PSF (at 1.5 keV, for example, ∼90 per cent of the energy is expected to fall within only 4 pixels), and the presence of the strong and spatially-variable diffuse component.

For isolated sources, such as sources 1, 4, 5, 12, 13 and 14, the photometry suffers little from contamination by extended emission and therefore the profiles are reliable despite the small number of counts detected for some of the sources. All sources show profiles consistent with the model PSF, although source 5 shows some evidence for an extended component. However, as this is based on only one data point, we will assume that all isolated sources are indeed unresolved.

The scenario is less straightforward for those sources located in the innermost region of the galaxy since the background estimates will not account for any spatial changes of the diffuse emission within the apertures used to obtain the profiles. Fig. 2 shows that while the spatial distribution of sources 3, 6, 8 (the southern nucleus), 11 and 13 are well described by the model PSF, sources 2, 7 (the northern nucleus), 9 and 10 are clearly resolved.

A simple Gaussian fit to the profiles shown in Fig. 2 gives FWHM values (the only parameter allowed to vary during the fitting) of ∼ 0.8–1.5 pixels (∼ 0.4–0.7 arcsec) for unresolved sources, while extended sources had FWHM ∼ 2.2–2.8 pixels (implying deconvolved FWHM ∼ 1.8–2.5 pixels or ∼ 0.9–1.3 arcsec). The model

Table 1. Detected discrete sources in NGC 3256. Background-subtracted source counts (SCs) above 0.3 keV are given for each source. The significance of the detections was determined as (source counts/σ_B), where σ_B is the standard deviation of the background and was computed as $1 + \sqrt{\text{Background counts} + 0.75}$. This correction to the standard deviation gives a more appropriate estimate of Poissonian errors for cases of low number counts (Gehrels 1986).

Source	Position (J2000)	Source counts	Significance
1	10 27 48.02 −43 54 26.5	22.8 ± 6.2	25.34
2	10 27 50.04 −43 54 20.5	50.6 ± 10.9	18.58
3	10 27 50.74 −43 54 16.2	38.7 ± 12.8	11.53
4	10 27 50.93 −43 53 43.4	25.6 ± 7.0	19.15
5	10 27 51.23 −43 53 58.8	59.7 ± 11.0	24.00
6	10 27 51.23 −43 54 10.9	92.4 ± 17.3	18.27
7(N)	10 27 51.25 −43 54 14.2	712.2 ± 30.6	141.38
8(S)	10 27 51.22 −43 54 19.4	34.3 ± 13.0	10.09
9	10 27 51.64 −43 54 09.7	171.2 ± 18.9	36.27
10	10 27 51.76 −43 54 13.6	261.6 ± 20.7	60.05
11	10 27 52.03 −43 54 12.6	119.8 ± 15.1	38.84
12	10 27 52.56 −43 53 49.9	48.3 ± 8.5	42.84
13	10 27 52.88 −43 54 11.8	26.7 ± 7.9	14.51
14	10 27 55.14 −43 54 47.1	88.5 ± 10.7	86.00

Downloaded from http://mnras.oxfordjournals.org/ at University of Durham on August 8, 2014

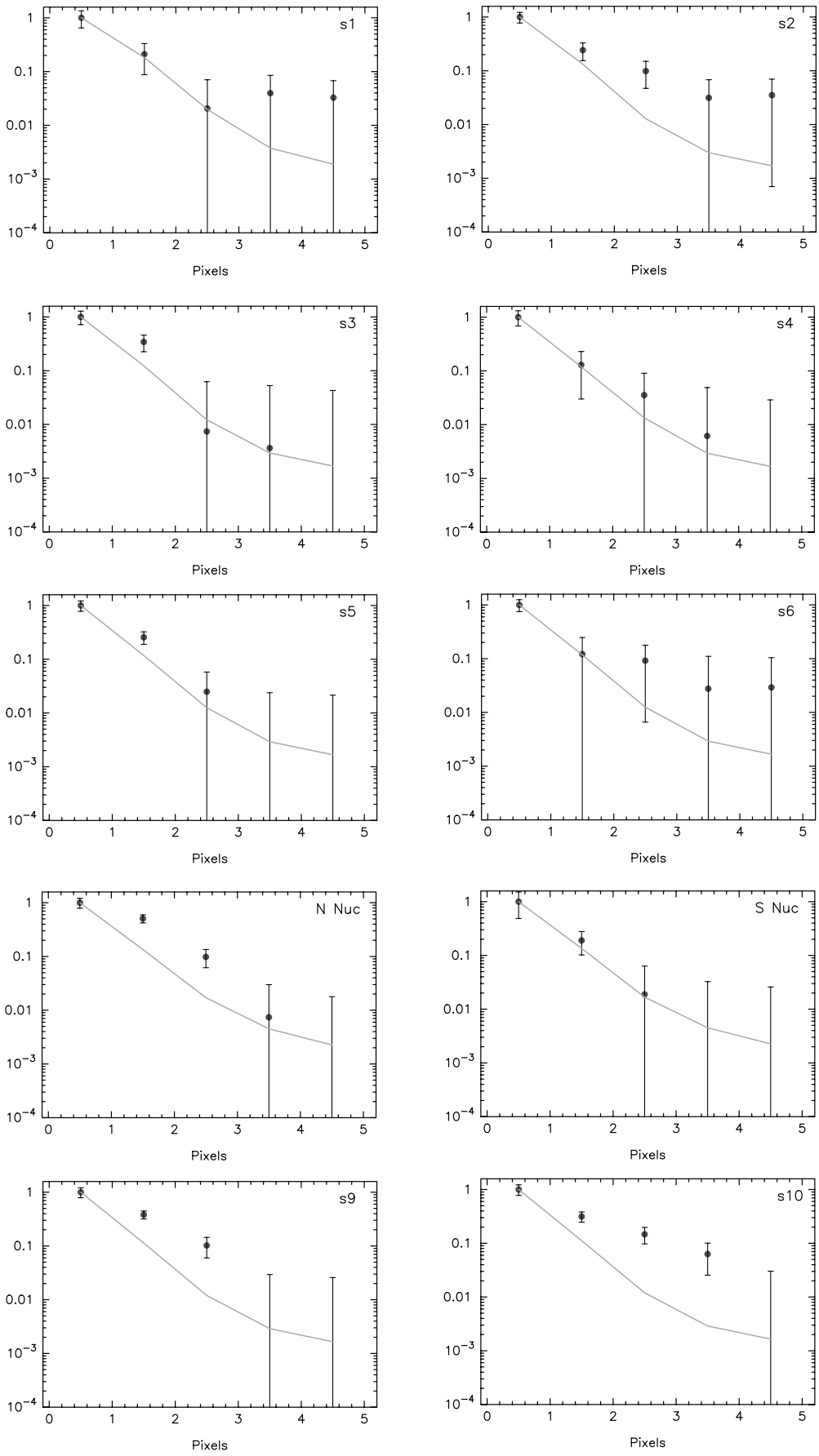

Downloaded from http://mnras.oxfordjournals.org/ at University of Durham on August 8, 2014

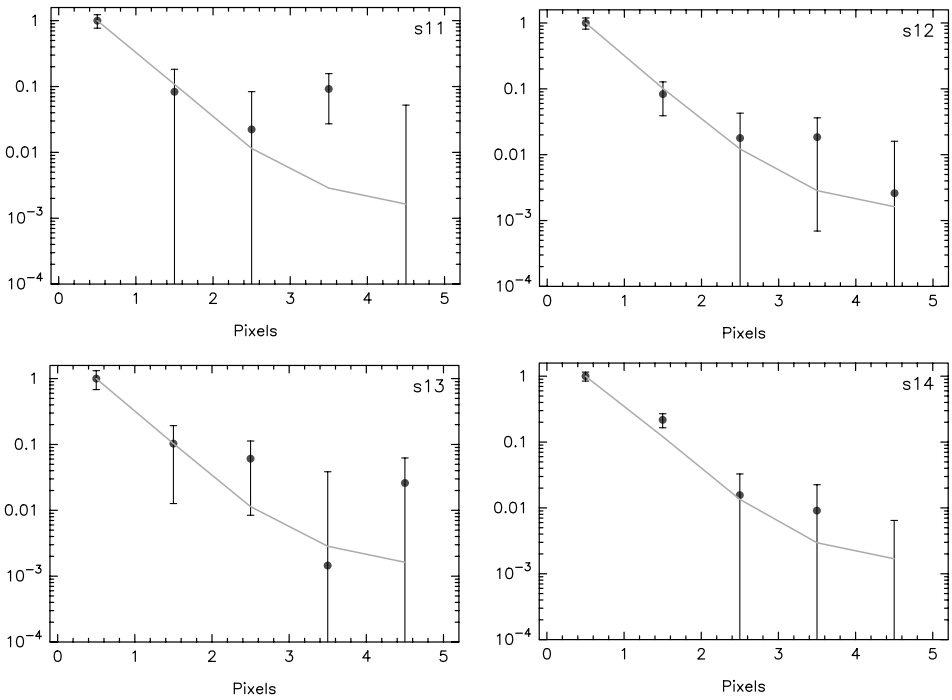

Figure 2. Spatial profiles of the discrete sources obtained from a full 0.3–10 keV band image are compared with the model PSF (continuous lines). The error bars correspond to 1σ confidence levels. The profiles for both nuclei (N and S) were obtained from a harder, 2–5 keV image.

PSF had a FWHM $\sim$ 1.2 pixels ($\sim$ 0.6 arcsec). The only source that did not follow this trend was source 2, which has a best-fit value of 1.5 pixels (i.e. within the range of the unresolved sources), even though Fig. 2 suggests that the profile is extended.

The aperture used to perform the count subtraction ($r =$ 3.5 pixels) is only adequate if it contains most of the flux from the extended sources. The Gaussian fit to the profiles shows that these sources have a FWHM of up to 2.8 pixels (i.e. $3\sigma = 3.6$ pixels or $\sim$ 1.8 arcsecs). A well-centred extraction aperture of 3.5 pixels, therefore, will contain most of the source counts. Since all extended sources show a well-defined peak, and sources 7, 9 and 10 correspond to the brightest discrete sources found in the galaxy, the centring of their flux distribution is well determined and, therefore, these apertures were adequate.

3.2 Fluxes and luminosities

Only three of the 14 detected discrete sources had sufficiently high numbers of counts to perform a useful spectral analysis. These correspond to source 7, the northern nucleus, and sources 9 and 10. The spectra were modelled with a single [Mekal (M) or power-law (PL)] component and a double [Mekal and power-law (M + PL)] model in the 0.5–10 keV passband. These models are representative of sources dominated by thermal emission (such as SNRs and galactic bubbles), non-thermal emission (such as accreting compact objects), and composite objects.

For all sources, the single Mekal model was a very poor representation of the data, while the single power law gave a much better fit, particularly for source 9, given the low number of bins available (see Table 2 and Fig. 3). For sources 7 and 10, M + PL models were also tried. For source 7 two independent hydrogen columns were adopted for each spectral component in model *c*. This model represents a physically plausible scenario with the low-temperature Mekal component representing a large-scale extended gaseous phase, and the harder, more-absorbed component arising from embedded or intrinsically absorbed sources directly associated with the northern nucleus. Since the best-fit values of the hydrogen column affecting the low-temperature Mekal component were very close to or slightly less than Galactic, we fixed the $N_{\rm H}$ to the Galactic column (see the footnote to Table 2), resulting in the same number of degrees of freedom as model *b*.

To convert the count rates to fluxes for the remaining sources we must assume an intrinsic spectral shape and intervening absorbing column. In order to gain some insight into the best values to adopt, we studied the X-ray colours of the sources, defined as the ratio of counts observed in the 0.3–1.0, 1.0–2.0 and 2.0–7.0 keV energy bands. The bands were chosen in order to maximize the detection of the sources in all three bands, as well as to obtain a good characterization of the spectra. To compare the observed X-ray colours of the sources with different spectral shapes, we computed the colours of pure power law and Raymond Smith models using the HEASRAC Portable, Interactive, Multi-Mission Simulator (PIMMS – Mukai 1993).

Grids of points were determined for parameters $\Gamma = 0.5$–3.0 and $kT = 6.0$–0.5 keV, for the power law and Raymond Smith models, respectively, and for $N_{\rm H} = 10^{21}$–10^{23} cm^{-2}. In Fig. 4 we have plotted the computed grids along with the observed colours of the discrete sources. Error bars were computed as one standard deviation in the count ratios. The southern nucleus (source 8) is not shown since it is not detected in either of the two softest bands used in the diagram (see further discussion below in this section).

The positions for sources 7, 9 and 10 can be used to investigate the limitations of using this type of diagram, since we have determined the spectral parameters from spectral fits. From the single power-law fits shown in Table 2, we find that all sources have an absorbing column higher than Galactic but lower than 5×10^{21} cm^{-2}, in agreement with the location of the sources in the colour–colour diagram. However, from the diagram the columns

Downloaded from http://mnras.oxfordjournals.org/ at University of Durham on August 8, 2014

Table 2. Fitted models for the emission from sources 7 (the northern nucleus), 9 and 10. Hydrogen columns are given in units of $10^{21}\,\mathrm{cm}^{-2}$ and plasma temperatures in units of keV. The errors correspond to 90 per cent CL for 1 parameter of interest. *Observed* fluxes are in units of $10^{-14}\,\mathrm{erg\,s}^{-1}\,\mathrm{cm}^{-2}$ and *intrinsic* luminosities are in units of $10^{40}\,\mathrm{erg\,s}^{-1}$ (for an assumed distance of 56 Mpc).

Source	Model	$N_{\rm H}$	kT	$N_{\rm H}$	Γ	$\chi^2_{\rm red}$(dof)	$F_{\rm x}$ 0.5–2.5 (keV)	$L_{\rm X}$ 0.5–2.5 (keV)	$F_{\rm x}$ 2.5–10 (keV)	$L_{\rm X}$ 2.5–10 (keV)
7(N)	PL	–	–	$3.8^{+0.8}_{-0.6}$	$2.81^{+0.35}_{-0.28}$	1.81(32)	6.77	6.88	3.90	1.52
7(N)	M + PL[a]	$3.4^{+1.0}_{-0.9}$	$0.66^{+0.12}_{-0.10}$	†	$2.25^{+0.38}_{-0.24}$	0.91(30)	6.64	5.68	4.80	1.85
7(N)	M + PL[b]	Gal	$0.69^{+0.10}_{-0.06}$	$5.8^{+8.0}_{-2.3}$	$2.57^{+0.81}_{-0.33}$	0.84(30)	7.01	8.50	4.53	1.79
9	PL	–	–	$1.6^{+2.1}_{\rm Gal}$	$2.43^{+1.09}_{-0.80}$	1.04(10)	1.59	0.93	0.91	0.35
10	PL	–	–	$2.9^{+2.0}_{-1.7}$	$2.91^{+1.20}_{-0.81}$	1.51(13)	2.38	2.08	0.73	0.28
10	M + PL	Gal	$1.00^{+0.18}_{-0.23}$	†	$1.67^{+0.40}_{-0.37}$	0.93(12)	2.55	1.15	1.28	0.44

[a,b] Single and double $N_{\rm H}$ columns, respectively.
†Same hydrogen column as applied to previous spectral component.
Throughout this paper, whenever the column of gas fitted to a low-temperature thermal component (probably associated with a large-scale extended hot phase) presented an unrealistically low value of $N_{\rm H}$, the Galactic hydrogen column ($N_{\rm Gal} \sim 9\times10^{20}\,\mathrm{cm}^{-2}$, labelled 'Gal') was adopted instead.

are underestimated for sources 7 and 10. For source 7 for example, $N_{\rm H} \sim 4\times10^{21}\,\mathrm{cm}^{-2}$ is found from the spectral fit, while the column deduced from the colour–colour diagram is about $10^{21}\,\mathrm{cm}^{-2}$. The fitted power-law indices also roughly agree with the location of sources 9 and 10, giving values of $\Gamma \sim 2.5$–3.0. A larger discrepancy is seen for source 7 where the power-law index estimated from the diagram is harder ($\Gamma \sim 2.0$–2.5) than its fitted value. These disagreements could be due to the observed spectral complexity of the emission in source 7, which cannot be recovered by the over-simplified single-parameter models used in the colour–colour diagram. For source 9, however – the only case where the single-power-law model gives an acceptable fit ($\chi^2_{\rm red} \sim 1.0$) – the best-fit values suggest a hard source and a moderate hydrogen column ($\Gamma \sim 2.4$, $N_{\rm H} \sim 1.6\times10^{21}\,\mathrm{cm}^{-2}$), which is not accurately reflected by the position of the source in the colour–colour diagram. These comparisons clearly illustrate the limits of using colour–colour and hardness-ratio diagrams.

The positions of the remaining sources in the colour–colour diagram show that most of the sources have an absorbing column above the Galactic value, i.e. between 10^{21} and $5\times10^{21}\,\mathrm{cm}^{-2}$. The bulk of the sources show a harder spectral shape than those for which we have performed a spectral fitting and therefore a power law with index between $\Gamma = 2.0$ and 2.5 seems a reasonable spectral shape to adopt. Bearing in mind the limitations in obtaining spectral parameters from the colour–colour diagram as discussed above, the derived power-law indices are in good agreement with that expected from a population of high-mass X-ray binaries ($\Gamma \sim 1$–2 : White, Nagase & Parmar 1995) or young supernova remnants ($kT \sim 1$–4 keV : Bregman & Pildis 1992). Sources 2 and 3, however, do not follow the trend shown by the rest of the sources and present evidence for much larger absorption.

These sources are not detected in the 0.3–1.0 keV band and we only have an upper limit for their (0.3–1.0 keV)/(1.0–2.0 keV) colour. A column density of $10^{22}\,\mathrm{cm}^{-2}$ was chosen as a representative value for these two heavily-absorbed sources.

In order to check that the range of power-law indices and absorbing columns inferred from the colour–colour diagram are representative of 'real' spectral shapes, we produced two 'stacked' spectra for a group of obscured and unobscured sources. The sources were selected based on their observed colours in Fig. 4 and from their location with respect to the reddening observed in a colour image of the central region of the galaxy (see Section 6.2). Fig. 5 clearly shows that although the observed hard tails present a similar slope for the two stacked spectra, the soft end shows clear evidence for significant absorption in these sources, in good agreement with their position in the colour–colour diagram. Single-component models (M or PL) were fitted to the stacked data and showed that the absorbing column affecting the unobscured sources was a few times the Galactic value, while the corresponding value for the obscured sources was about an order of magnitude larger.

The southern nucleus is only detected at hard energies, and no counts are detected below ~2.0 keV. This is perhaps not surprising, since it is well established that this is a heavily obscured region. To characterize the spectral shape of this nucleus we have again used a colour–colour diagram, but this time using the 2.0–3.3, 3.3–4.5 and 4.5–10 keV energy ranges. The bands were chosen in order to maximize the background-subtracted number of counts in each one of them. We then compared the observed (2.0–3.3 keV)/(3.3–4.5 keV) and (4.5–10 keV)/(3.3–4.5 keV) colours with grids of power-law models as described previously. We find that the spectral shape of the source is well parametrized by a range of indices $\Gamma \sim 1.0$–2.5 if an absorbing column of $5\times10^{22}\,\mathrm{cm}^{-2}$ is adopted. A higher column ($10^{23}\,\mathrm{cm}^{-2}$) is possible, but only if $\Gamma \gtrsim 2.0$, while a lower column ($10^{22}\,\mathrm{cm}^{-2}$) requires $\Gamma \lesssim 1.5$. Columns above $10^{23}\,\mathrm{cm}^{-2}$ or below $10^{22}\,\mathrm{cm}^{-2}$ are not consistent with the observed colours.

The final computed fluxes and luminosities for all sources are listed in Table 3. They were computed assuming a power-law spectrum with indices $\Gamma = 2.0$ and 2.5 and the hydrogen columns discussed above. The adoption of the different indices implies changes in the fluxes of about ~30 per cent. Much larger errors could be introduced if the spectral shapes are not well described by the assumed models, as can be seen by comparing the fluxes and luminosities obtained for source 7 from the spectral fitting and the adopted parameters used in Table 3. Statistical errors will dominate, however, for the faintest sources ($\lesssim$30 counts – see Table 1). Another significant source of uncertainty is the adoption of a representative background. This problem is particularly important for sources embedded in strong diffuse emission. In all, the fluxes and luminosities in Table 3 are probably good to within a factor of two or three. Inspection of Tables 1 and 3 shows that our sensitivity threshold is $\sim 4\times10^{-15}\,\mathrm{erg\,s}^{-1}\,\mathrm{cm}^{-2}$

Downloaded from http://mnras.oxfordjournals.org/ at University of Durham on August 8, 2014

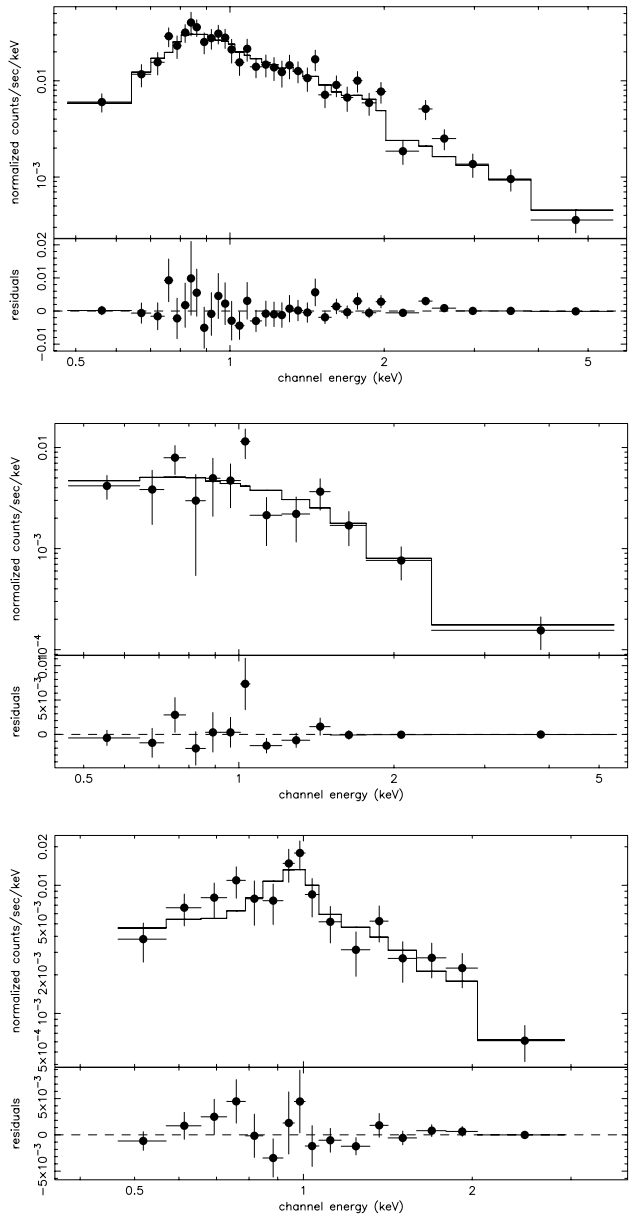

Figure 3. Spectra of the three brightest discrete sources in NGC 3256 in the 0.5–10 keV range: source 7 (the Northern nucleus – top), 9 (centre) and 10 (bottom). The top panels of each plot show the data and folded model (see Table 2). The bottom panels show the residuals to the fit.

($\sim 1.5 \times 10^{39}$ erg s^{-1}) for an isolated source, and $\sim 1.5 \times 10^{-14}$ erg s^{-1} cm^{-2} ($\sim 6 \times 10^{39}$ erg s^{-1}) for sources embedded within the diffuse emission.

3.3 Time variability

In order to search for time variability of the discrete sources, light curves for the six brightest objects were constructed using 6 bins of 4.3 ks each, spanning a total of 26 ks. The errors associated with the count rates correspond to 1σ deviations assuming Poisson statistics. The light curves are shown in Fig. 6.

A superficial examination shows no obvious signs of variability in the lightcurves. We carried out a χ^2 test to compare the lightcurves with a constant distribution. The test showed that all distributions are consistent with no variability ($\chi^2_{\rm red} \lesssim 0.5$), except for source 6 where no variation is a poorer representation of the data ($\chi^2_{\rm red} = 1.59$). However, this is not a significant result, and the null hypothesis is not rejected at the 85 per cent confidence level.

4 DIFFUSE EMISSION

4.1 Integrated spectrum

In order to perform a spectral analysis of the diffuse component in NGC 3256 a large aperture with a diameter of 40 arcsec (~ 11 kpc) was defined after removing all discrete sources. At this distance from the central peak of emission the diffuse emission had a surface brightness comparable with the background. The large aperture used implies that the observed episodes of high background described in Section 2 could contaminate the intrinsic emission from the galaxy. Therefore the data were filtered to exclude background count rates above 1.5 counts per second. Consequently only 14.5 ks (~ 52 per cent) of the total observing time was used. These screened data are used for all the analysis described here and in Section 4.2.

The aperture was fully contained within only one (out of four) of the readout nodes of the S3 chip (node-to-node sensitivity changes can be as large 10 per cent). In fact, the bulk of the extended component covered a roughly circular region with a diameter $\lesssim 30$ arcsec, compact enough for the response of the detector to remain fairly constant. For this reason only one set of Fits Embedded Functions (FEFs – a FITS table that stores the mapping of the energy-to-pulse height) was used to calibrate the spectrum. (Using a response built up from the weighted combination of the 3 to 4 FEFs that fully covered the area subtended by the diffuse component did not change the fit to the data.) The background was obtained from a large semi-annular region surrounding NGC 3256 ($r \sim 75$–115 arcsec) and fully contained within the same readout node as the emission from the galaxy.

Fig. 7 shows the spectrum of the diffuse emission. A total of ~ 2860 counts were detected within the aperture, of which at most ~ 100 could be from the background. The relative softness of the emission is evident as no counts are detected above ~ 5 keV. The presence of strong emission lines is also readily visible at ~ 1.4 and ~ 1.8 keV. At these energies we expect contributions from lines such as He-like and K-shell emission of Mg and Si ions, indicating the presence of a thermal component with $kT < 2$ keV.

The spectrum of the diffuse emission was first fitted using single- and double-component models, which yielded unacceptable chi-squared values. We then followed with three-component models (M + M + M or M + M + PL). The presence of multi-temperature gas has already been claimed for several starburst galaxies, such as NGC 1808 (Awaki et al. 1996), Arp 299 (Heckman et al. 1999), NGC 4449 (della Ceca, Griffiths & Heckman, 1997), NGC 253 and M82 (Ptak et al. 1997). The introduction of a power-law component could account for an unresolved population of accreting binaries. Since different spectral components can have different degrees of absorption (see references above), we allowed for different $N_{\rm H}$ values for the fitted components. We also fixed the hydrogen column absorbing the softest thermal-plasma component to the Galactic value, since fitting the parameter nearly always resulted in a Galactic or slightly under-Galactic value.

The results of the spectral fits are reported in Table 4. Solar metallicities were assumed throughout, consistent with the optically-measured abundances (Lípari et al. 2000). If left free to

Downloaded from http://mnras.oxfordjournals.org/ at University of Durham on August 8, 2014

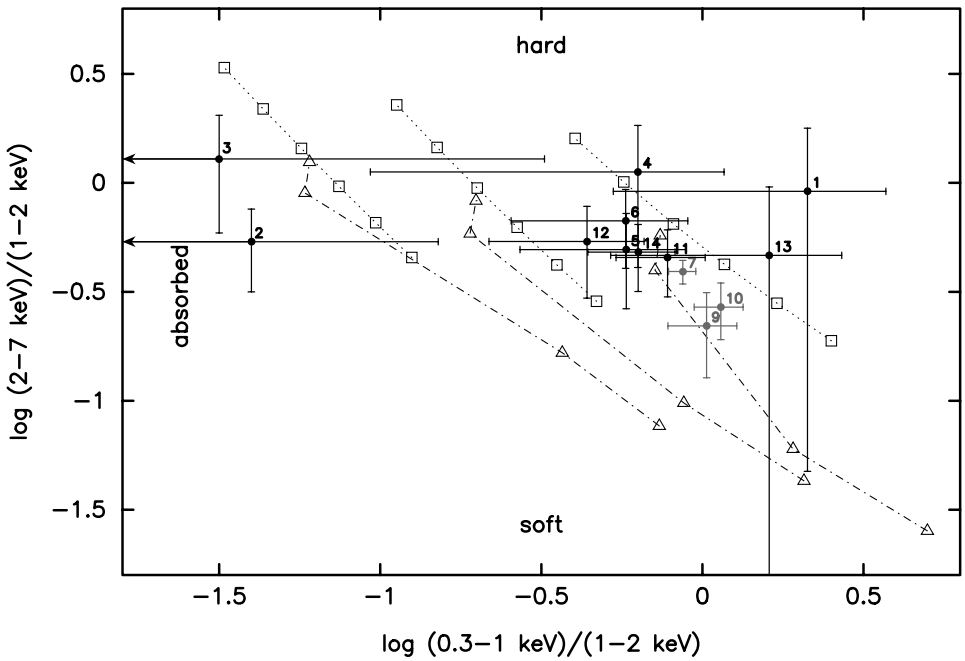

Figure 4. 'Hardness-ratios' (colour–colour) diagram for X-ray discrete sources. The X-ray colours were defined as the ratio of counts observed in the 0.3–1.0, 1.0–2.0 and 2.0–7.0 keV energy bands. One σ error bars are shown. The grids of models correspond to single Raymond–Smith plasmas (triangles – dash–dotted line) with temperatures (from top to bottom) 6.0, 3.0, 1.0 and 0.5 keV, and single power laws (squares – dotted line) with index Γ (from top to bottom) 0.5, 1.0, 1.5, 2.0, 2.5 and 3.0. From right to left, successive grids correspond to absorbing columns of 10^{21} (just above Galactic), 5×10^{21} and $10^{22}\,\mathrm{cm}^{-2}$, respectively. Sources 7, 9 and 10, for which spectral fits were properly derived, are also included.

vary, the abundances imply a solar or over-solar value, without significantly improving the fit. For the first two models in Table 4, the second and third spectral components are subject to the same hydrogen column. For the third and fourth model, each component has an independent intervening N_{H}. Despite the clear improvement in the statistics of the successive models presented in Table 4, it was impossible to reduce χ^2_{red} below 1.3. This is probably due to the still preliminary status of the instrument responses available for the calibration of the data. The uncertainties mostly affect the modelling of line-emission-dominated spectra. All the models in Table 4 are consistent with a general picture of a moderately-absorbed cool thermal plasma plus a warmer thermal component with a much higher absorption. A steep power law or a thermal component with a temperature of about 4 keV is necessary to explain the faint hard tail seen in the spectrum. Table 5 lists fluxes and luminosities derived for each component from the model with the best reduced chi-squared (M + M + PL model; last entry in Table 4).

4.2 Spatially-resolved spectra

The spectral-imaging capabilities of *Chandra* enable a more detailed study of the diffuse emission. Ideally, we would like to identify each of the spectral components determined in the previous section with a specific spatial region, but this is only possible if each component strongly dominates the local emission.

Two thermal components have been clearly identified in the *Chandra* data. Observational evidence on galactic winds suggests that the central regions of starbursts are characterized by higher plasma temperatures than the outer regions (Strickland, Ponman & Stevens 1997; Pietsch et al. 2000). This is also supported by various theoretical models of galactic winds (Suchkov et al. 1996; Chevalier & Clegg 1985). Given the nearly face-on orientation of NGC 3256 we decided to extract spectra from annular regions centred in between both nuclei. After experimenting with different radii we defined three regions, A, B and C with outer radii of 15, 23 and 40 pixels ($\sim$ 4, 6 and 11 kpc). This choice gives a similar number of counts ($\sim$ 900–1000) in each region and also provides a good representation of the spectral changes with radius. Region C is roughly coincident (although with a larger outer radius) with the onset of a ring of broad Hα line emission (FWZI up to $\lesssim 6000\,\mathrm{km\,s}^{-1}$) probably associated with the wind, as discussed by MLH.

The regions are shown in Fig. 8 overlaid onto a smoothed image of the X-ray emission. The spectra obtained for each region (after removing the discrete sources) are also shown. The spectra show that while the emission above 1 keV shows a similar trend for all radii, the dispersion is much larger below 1 keV, suggesting that

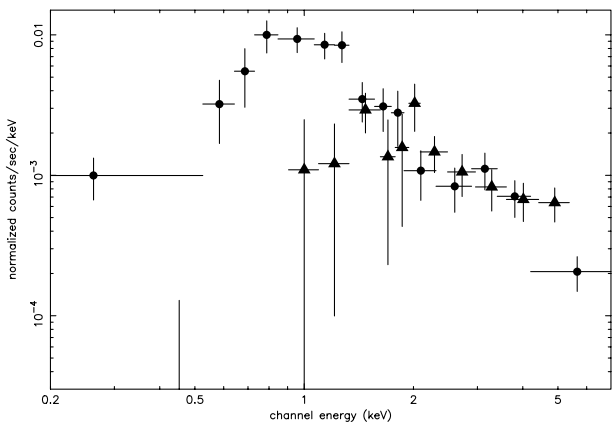

Figure 5. Stacked spectra for heavily-absorbed sources 2, 3 and 8 (triangles), and less-absorbed sources 5, 6, 11 and 13 (circles).

Downloaded from http://mnras.oxfordjournals.org/ at University of Durham on August 8, 2014

Table 3. Fluxes and luminosities in the 0.5–10 keV energy range for the compact sources assuming a single power-law component with index $\Gamma = 2.0$ and 2.5. The adopted hydrogen columns are also given. *Observed* fluxes are in units of 10^{-14} erg s^{-1} cm^{-2} and *intrinsic* luminosities are in units of 10^{40} erg s^{-1} (for an assumed distance of 56 Mpc).

		$\Gamma = 2.0$		$\Gamma = 2.5$	
Source	N_H	F_x	L_X	F_x	L_X
1	10^{21}	0.43	0.19	0.30	0.14
2	10^{22}	2.12	1.38	1.59	1.43
3	10^{22}	1.62	1.05	1.22	1.10
4	5×10^{21}	0.81	0.45	0.59	0.42
5	10^{21}	1.13	0.49	0.78	0.36
6	5×10^{21}	2.91	1.63	2.20	1.58
7(N)	10^{21}	13.5	5.80	9.25	4.29
8(S)	5×10^{22}	3.00	3.04	2.47	4.10
9	10^{21}	3.25	1.39	2.22	1.03
10	10^{21}	4.96	2.13	3.40	1.58
11	10^{21}	2.27	0.97	1.56	0.72
12	5×10^{21}	1.52	0.85	1.10	0.79
13	10^{21}	0.51	0.22	0.35	0.22
14	5×10^{21}	2.78	1.56	2.02	1.45
Total		40.81	21.15	29.05	19.21

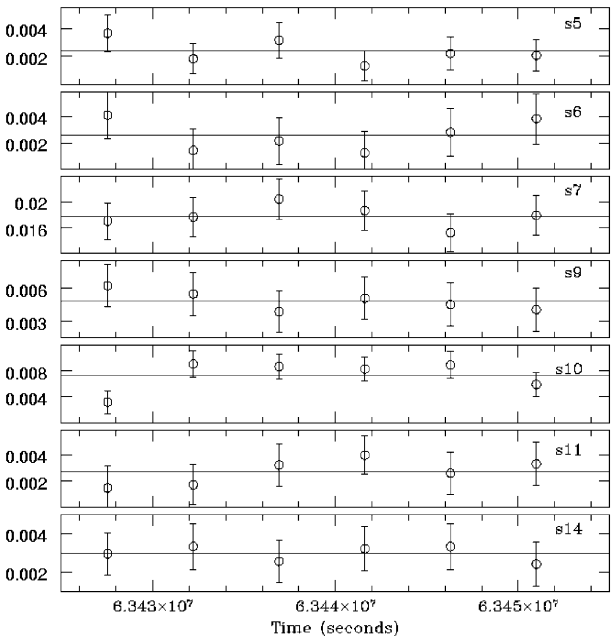

Figure 6. Discrete-source lightcurves. The average count rate for each source is plotted as a straight line.

different amounts absorption and/or peak temperatures may characterize the different regions.

In order to quantify the different spectral trends observed in Fig. 8 we fitted each spectrum to a thermal plasma plus a power law (M + PL), each component absorbed by an independent hydrogen column. The power-law component was fixed with an index of 2.7. The results are shown in Table 6. The best-fit value for the hydrogen column affecting the thermal plasma in region C was very close to Galactic and therefore, given that a column much larger than Galactic is unlikely to pertain across such an extended region, a value of 'Gal' (see the footnote to Table 2) was adopted.

The results in Table 6 show a trend of the spectral parameters with radius. The most robust result concerns the amount of extinction affecting each region, with N_H varying by about an order of magnitude between the central and the outer parts of the diffuse emission. The variation in temperature is less certain given the associated errors. However, the presence of a ~ 0.9 keV highly-absorbed plasma has been well established by *ASCA* observations (see Section 5). So the correlation of higher temperatures with higher N_H supports this result. Furthermore, we also extracted a spectrum from a smaller ($r = 10$ pixels, ~ 3 kpc) circular region which is not shown in Fig. 8. The fit to the data (using the same model as for the other regions) gives $N_H 11^{+6}_{-3} \times 10^{21}$ cm^{-2} and $kT 0.9^{+0.2}_{-0.3}$ keV for the column and temperature of the thermal plasma, respectively. The large errors reflect the poor statistics (only 13 bins were obtained; $\chi^2_{red} = 0.9$) but it again supports the trend found in Table 6.

The quantitative results presented in Table 6 should be treated with caution. For example, the derived 0.5–10 − keV flux for the central region (A) accounts for less than half of the flux determined for the 0.9-keV component (see Table 5), which is thought to dominate in this region. The use of over-simplified and poorly-constrained models to characterize the different emitting regions is probably responsible for part of the disagreement. However, it is also clear that the two thermal components observed in the integrated spectrum of the diffuse emission are not representative of the spectral complexity present on small scales; they only characterize the average properties of the emission. It is not possible to explore these important issues further with the present data, but a significantly longer exposure would no doubt answer some of the open questions.

5 COMPARISON WITH *ASCA* OBSERVATIONS

MLH have reported *ASCA* observations of NGC 3256 and determined a total luminosity for the system of $\sim 1.6 \times 10^{42}$ erg s^{-1} in the 0.5–10 keV energy range. In comparison, Tables 2 and 3 imply a total luminosity of $\sim 9 \times 10^{41}$ erg s^{-1} in the same spectral range as determined with *Chandra*, i.e. a reduction of $\sim$40 per cent in luminosity. We should attempt to understand the origin of this difference.

Given the extremely low spatial resolution of the *ASCA* (PSF FWHMS ~ 3 arcmin), the spectral analysis presented by MLH corresponds to the integrated emission (i.e. diffuse plus compact sources) of most of the galaxy. Their adopted model consists of two thermal plasmas ($kT \sim 0.3$, 0.8 keV) and a power law with photon index $\sim$1.7. The power law and the high-temperature thermal components are affected by a single absorbing column of $\sim 8 \times 10^{21}$ cm^{-2}. This model, however, is not a good description of a *Chandra* spectrum obtained from the total emission observed within the central 40 arcsec of the galaxy. A model using the best-fit values derived by MLH gives an unacceptable fit ($\chi^2_{red} = 1.7$). In fact, if the parameters are allowed to vary (and a Mekal component is used to described the thermal emission instead of a Raymond–Smith plasma, as used by MLH), the best-fit values for the *Chandra* 'total spectrum' are very similar to those found for the diffuse emission only (compare Table 4 and Table 7), although a flatter power law is determined for the total spectrum, as expected from the hard spectrum that characterizes the discrete sources. From this fit we derive an *observed* flux of $\sim 1.2 \times 10^{-12}$ erg s^{-1} cm^{-2} in the 0.5–10 keV energy band, which differs by only ~ 5 per cent from the flux derived from the *ASCA* observations.

The difference in the models adopted in the analysis of the *ASCA*

Downloaded from http://mnras.oxfordjournals.org/ at University of Durham on August 8, 2014

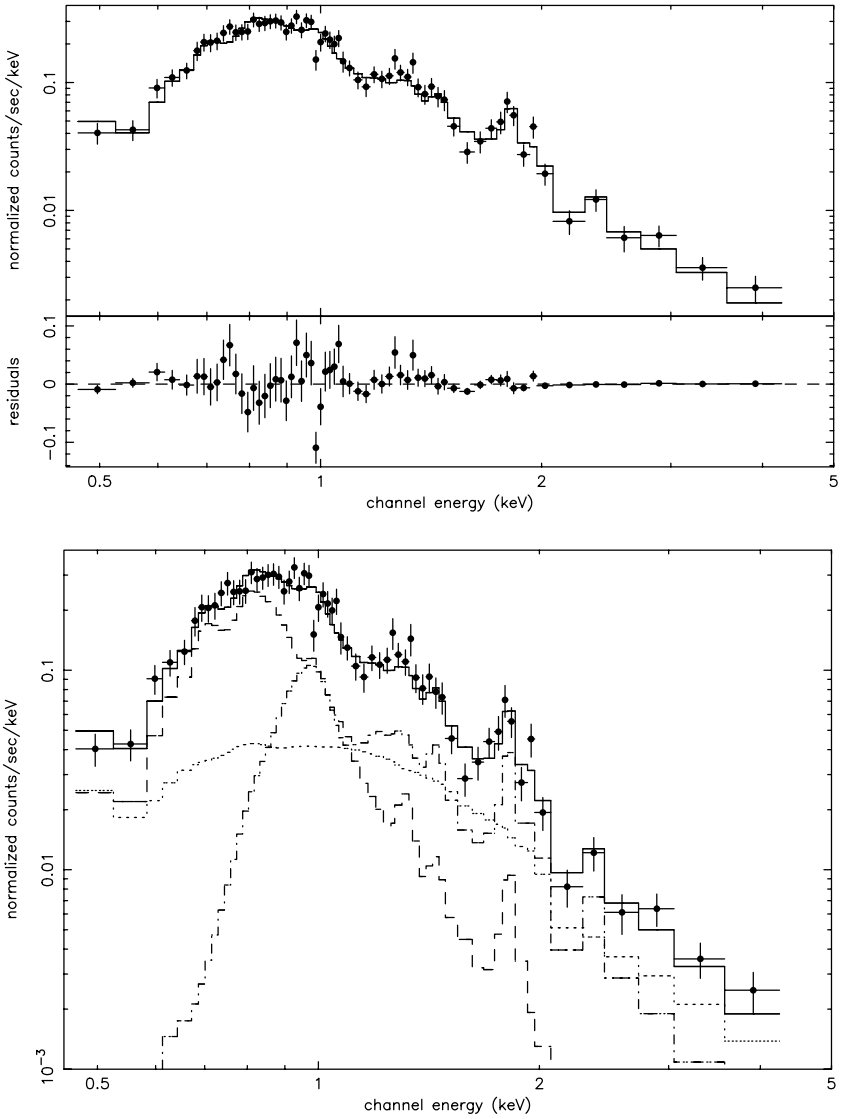

Figure 7. Left: spectrum of the diffuse component in NGC 3256 in the 0.5–5 keV range. The top panel shows the data and folded model; the bottom panel shows the residuals in the same energy range. Right: best-fit model components.

and *Chandra* data can explain the different derived *intrinsic* fluxes and luminosities. The change is primarily due to the reduction in the intrinsic emission (or component normalization) of the warm, 0.8–0.9 keV, component, as seen by *Chandra*, which is the most luminous component in the model derived by MLH. Inspection of fig. 7b in MLH clearly shows a warm component that is dominant in the 1–2 keV range, since the contribution from a heavily-absorbed power-law component is almost negligible at these

Table 4. Best-fit model parameters for the diffuse emission in the 0.5–10 keV energy range. Solar abundances were assumed for the Mekal components. Intervening hydrogen columns are in units of 10^{21} cm^{-2} and plasma temperatures are in units of keV. 'Gal' stands for a foreground Galactic hydrogen column (9×10^{20} cm^{-2}). Errors correspond to 90 per cent CL for 1 parameter of interest. *Observed* fluxes are in units of 10^{-13} erg s^{-1} cm^{-2} and *intrinsic* luminosities are in units of 10^{41} erg s^{-1} (for an assumed distance of 56 Mpc).

Model	$N_{\rm H}$	kT	$N_{\rm H}$	kT	$N_{\rm H}$	kT or Γ	$\chi^2_{\rm red}$(dof)	$F_{\rm x}$	$L_{\rm X}$
M + M + M	Gal	$0.37^{+0.04}_{-0.03}$	$7.1^{+1.1}_{-1.0}$	$0.76^{+0.04}_{-0.05}$	†	$2.76^{+1.90}_{-0.67}$	1.54(59)	6.78	8.32
M + M + PL	Gal	$0.54^{+0.18}_{-0.13}$	$4.6^{+1.5}_{-1.2}$	$0.89^{+0.13}_{-0.19}$	†	$3.03^{+0.25}_{-0.49}$	1.45(59)	6.62	5.73
M + M + M	Gal	$0.60^{+0.04}_{-0.05}$	$9.7^{+1.8}_{-1.6}$	$0.90^{+0.10}_{-0.07}$	Gal$^{+0.8}$‡	$3.93^{+4.54}_{-1.14}$	1.36(58)	6.83	7.23
M + M + PL§ Gal $0.60^{+0.04}_{-0.07}$	$9.2^{+2.2}_{-2.2}$	$0.91^{+0.14}_{-0.09}$	$3.4^{+1.3}_{-1.8}$	$2.75^{+0.49}_{-0.68}$	1.31(58)	6.60	6.79		

† Same hydrogen column as applied to previous spectral component.
‡ The best-fit value of $N_{\rm H}$ was found to be slightly under Galactic.
§ Model component normalizations: 1.1×10^{-4} and 4.9×10^{-4} for the 0.6 and 0.9 keV Mekal components, respectively, in units of $(10^{-14}/4\pi D^2) \times \int n_{\rm e}^2\, {\rm d}V$ (where D is the distance to NGC 3256 in cm, $n_{\rm e}$ is the electron density in cm^{-3}, and V is the volume of the emitting region in cm^3); 1.5×10^{-4} for the power law, in units of 10^{-4} photons cm^{-2} s^{-1} keV^{-1}.

Downloaded from http://mnras.oxfordjournals.org/ at University of Durham on August 8, 2014

energies. The *Chandra* data, on the other hand, is consistent with a less-absorbed and stronger power-law component, implying a smaller contribution from the warm thermal component to the overall emission.

6 DISCUSSION

6.1 The double nuclei

6.1.1 Optical, infrared and X-ray properties

Optical and near-infrared observations show that the properties of the northern nucleus of NGC 3256 correspond to those of a strong starburst. Lípari et al. (2000) found that the optical-emission-line features correspond to 'those of low-ionization and high metallicity giant H II regions'. On the other hand, the outer regions ($R >$ 10 arcsec) are characterized by shock excitation (Lípari et al. 2000; MLH). Lípari et al. also presented UV spectra of the central region (10×20 arcsec) showing strong absorption lines, implying the presence of massive young stars. Kotilainen et al. (1996) obtained near-infrared emission line maps of the centre of the galaxy and determined an extinction towards the northern nucleus of $A_V \sim 2.4$ mag.

The southern nucleus of NGC 3256 was first imaged in the near-infrared continuum by Moorwood & Oliva (1994), although near-infrared spectroscopy of the source had already been presented by Doyon et al. (1994). From their *K*-band imaging, Moorwood & Oliva detected an obscured source located 5 arcsec to the south of the central peak (the northern nucleus) and suggested that this secondary peak corresponds to the nucleus of the merging companion galaxy. Support came with radio observations reported by Norris & Forbes (1995) showing two equally bright knots of emission. Near-infrared observations by Kotilainen et al. (1996) showed that the luminosity of both nuclei is comparable in the *L*-band (3.5 μm) and they estimated an extinction towards the southern nucleus of $A_V \sim 10$ mag. High-resolution *N*-band (12 μm) images show, however, that the northern nucleus is ~20 times brighter than the southern peak in the mid-infrared, suggesting that the northern nucleus is the dominant star-forming region in the galaxy (Lira & Ward 2002).

In order to improve the reddening estimations towards the galaxy nuclei, we have analysed archive *NICMOS* data of the central region of NGC 3256. These observations were obtained on 1997 November 28 using the NIC2 camera (FOV = 19.2×19.2 arcsec, FWHM for a point source ~0.15 arcsec) and the F222M (~*K*-band), F160W (~*H*-band), and F190N (Paα-plus-continuum at 1.90μm) filters. For details of the reduction procedure, see Alonso-Herrero et al. (2000). Gaussian fitting to the *K*-band data shows that both nuclei are resolved, with the northern nucleus (deconvolved FWHM ~ 0.25 arcsec) being more compact than the

Table 5. Fluxes and luminosities for the diffuse emission in the 0.5–10 keV energy range from the M + M + PL model. *Observed* fluxes are in units of 10^{-14} erg s^{-1} cm^{-2} and *intrinsic* luminosities are in units of 10^{41} erg s^{-1} (for an assumed distance of 56 Mpc).

Component	F_x 0.5–2.5 (keV)	L_X 0.5–2.5 (keV)	F_x 2.5–10 (keV)	L_X 2.5–10 (keV)
Cool Mekal	20.5	1.31	0.21	0.01
Warm Mekal	17.2	3.83	3.07	0.13
Power law	15.1	1.38	9.96	0.38
Total	52.8	6.26	13.2	0.52

Table 6. Best-fit parameters for the diffuse emission from regions A, B and C. A M + PL model was used with each component being absorbed by an independent N_H. The power-law component was frozen to a value of 2.7. Hydrogen columns are given in units of 10^{21} cm^{-2} and plasma temperatures in units of keV. The errors correspond to 90 per cent CL for 1 parameter of interest. *Observed* (i.e. uncorrected) fluxes in the 0.5–10 keV range for the thermal component only are given in units of 10^{-14} erg s^{-1} cm^{-2}.

Reg	N_H	kT	N_H	Γ	χ^2_{red}(dof)	F_x
A	$7.7^{+2.2}_{-2.4}$	$0.76^{+0.10}_{-0.16}$	$2.3^{+0.7}_{-0.6}$	2.7	1.08(29)	8.95
B	$2.8^{+1.5}_{-1.4}$	$0.60^{+0.05}_{-0.09}$	$4.3^{+1.6}_{-0.9}$	2.7	1.14(30)	8.61
C	Gal	$0.63^{+0.04}_{-0.04}$	$3.6^{+2.1}_{-0.9}$	2.7	1.18(34)	10.25

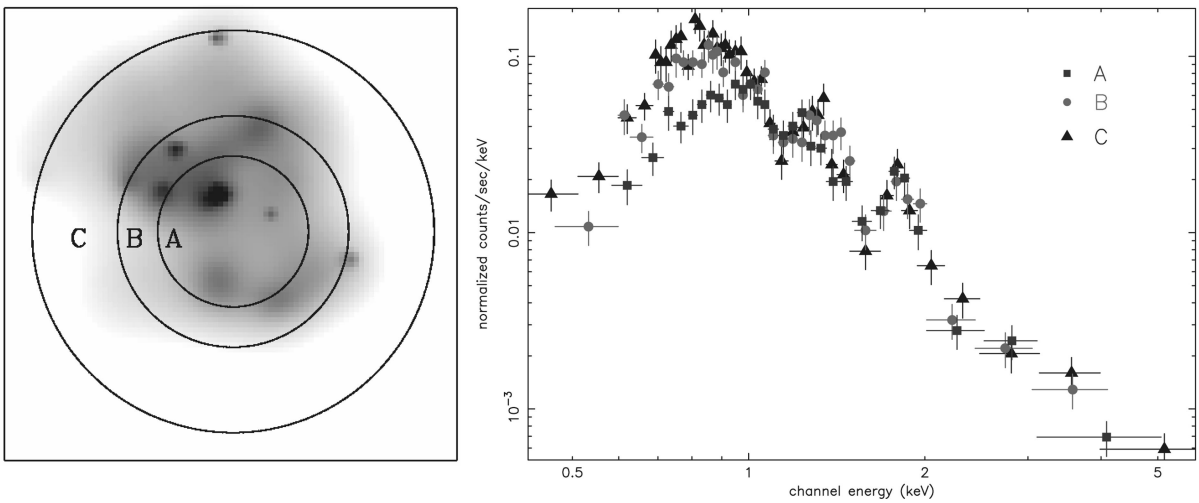

Figure 8. Left: smoothed X-ray image in the 0.3–1.5 keV energy range showing the regions defined for the spatially-resolved study of the diffuse emission. The radii of the regions correspond to ~4, 6 and 11 kpc. Right: spectra of the three regions in the 0.5–10 keV energy range.

Downloaded from http://mnras.oxfordjournals.org/ at University of Durham on August 8, 2014

southern nucleus (deconvolved FWHM ~ 0.34 arcsec). Using an aperture of 0.76 arcsec in diameter we measured an $H-K$ colour of 0.64 mag for the northern nucleus and 1.44 mag for the southern nucleus. Assuming a intrinsic colour $H-K \sim 0.22$ for the nuclei of starburst and Seyfert galaxies (Glass & Morwood 1985) and the extinction law of Cardelli, Clayton & Mathis (1989), this implies a visual extinction of ~ 5.5 and ~ 16 mag for the northern and southern nuclei, respectively. Assuming a Galactic gas-to-dust ratio, these values of A_V correspond to a hydrogen column density of $\sim 8\times10^{21}\,\mathrm{cm}^{-2}$ for the northern nucleus and $\sim 2.5\times10^{22}\,\mathrm{cm}^{-2}$ for the southern nucleus, in good agreement with the values inferred from the X-ray observations.

The northern nucleus is the brightest X-ray source in NGC 3256 with an unabsorbed luminosity of $\sim 8-10\times10^{40}\,\mathrm{erg\,s}^{-1}$ in the 0.5–10 keV energy range (see Table 2). The source is clearly resolved, and therefore it probably corresponds to a compact grouping of individual sources and diffuse emission at the heart of the nuclear starburst. The deconvolved FWHM of the radial profile in the 2–5 keV range shown in Fig. 2 corresponds to ~ 1 arcsec, or ~ 270 pc at the distance of NGC 3256. The full band, 0.5–10 − keV profile has a deconvolved FWHM of ~ 1.5 arcsec, corresponding to 400 pc, which is only a factor ~ 1.5 times smaller than the central starbursting region present in M82. The X-ray luminosities of both regions are also similar. In the case of M82, the 2–10 − keV emission is dominated by a highly variable and extremely luminous point source (Kaaret et al. 2001; Ward et al., in preparation).

The *NICMOS* data for NGC 3256 do not show conspicuous sources within a radius of 1.5 arcsec of the northern nucleus. The FWHM of the peak is only ~ 0.25 arcsecs or ~ 70 pc. Although there is little evidence for a one-to-one correlation between X-ray and infrared point sources, we would expect the overall size of these regions to be similar (e.g. M82 – Griffiths et al. 2000). Therefore any population of X-ray-emitting discrete sources (accreting binaries and compact SNRs) should be mainly associated with the very compact peak seen in the *NICMOS* data. It seems unlikely that a population of 'normal' binaries and SNRs could explain the observed X-ray emission, since several hundreds such sources would need to be packed within a very small volume. A more plausible scenario is that the X-ray emission is dominated by a diffuse component (e.g. the base of the galactic wind – support for this scenario comes from the rather steep index of the power-law component determined in Table 2, which can also be fitted by a hot-gas component with $kT \sim 2$ keV), and/or by a few nuclear ultraluminous sources.

6.1.2 *A hidden AGN?*

Many authors have searched for evidence of a hidden AGN in the heavily-obscured southern nucleus of NGC 3256. An active nucleus could play an important role in the energetics of the galaxy. So far observations at infrared and radio wavelengths have failed to provide unambiguous evidence for the presence of an AGN (Kotilainen et al. 1996; Norris & Forbes 1995). Mid-infrared *ISO* spectroscopy of NGC 3256 (Rigopoulou et al. 2000) also failed to detect the high-excitation emission lines indicative of the presence of an AGN. The large aperture of *ISO* may have completely diluted the emission from a hidden active nucleus, but even if this is the case it would imply an intrinsically weak AGN – which would not make a significant contribution to the total emission from the galaxy.

Our detection of the southern nucleus in X-rays allows us to address the AGN hypothesis from a different perspective. The unresolved nature of the source lends some support to the AGN scenario, although the small number of counts, coupled with the strong absorption, could conspire to hide any signature of an extended component. Adopting a power-law spectral model with $\Gamma = 2.0$ and an absorbing column of $5\times10^{22}\,\mathrm{cm}^{-2}$, we have determined an unabsorbed X-ray luminosity for the southern nucleus of $\sim 3\times10^{40}\,\mathrm{erg\,s}^{-1}$ in the 0.5–10 keV energy range (see Table 3). This is at least two orders of magnitude below the luminosities of 'classical' Seyfert nuclei (see for example George et al. 1998). To suppress the emission from such an active nucleus requires a much higher column than the one derived from either the *Chandra* or the *NICMOS* observations.

Alternatively, the observed X-rays could correspond to scattered emission from a Compton-thick Seyfert 2 nucleus. In this case, the direct emission from the primary source is suppressed by an extremely large intervening column ($N_{\mathrm{H}} > 10^{24}\,\mathrm{cm}^{-2}$) that is optically thick due to photoelectric absorption below ~ 10 keV and due to Compton scattered above ~ 10 keV. In these objects the central source can only be seen as a reflection component which, depending on the geometry and the physical conditions around the nucleus, can originate in either the torus (which is also probably responsible for the obscuration of the primary source) or a surrounding ionized medium.

However, one of the strongest indications of reprocessed X-ray emission in Compton-thick Seyferts is the presence of an iron line with an equivalent width > 1 keV at energies between 6 and 7 keV, depending on the ionization state of the scattering material (Matt et al. 2000; Maiolino et al. 1998). The large equivalent width is a

Table 7. Best-fit model parameters for the total emission in the 0.5–10 keV energy range. Solar abundances were assumed for the Mekal components. Intervening hydrogen columns are in units of $10^{21}\,\mathrm{cm}^{-2}$ and plasma temperatures are in units of keV. 'Gal' stands for a foreground Galactic hydrogen column ($9\times10^{20}\,\mathrm{cm}^{-2}$). Errors correspond to 90 per cent CL for 1 parameter of interest. *Observed* fluxes are in units of $10^{-13}\,\mathrm{erg\,s}^{-1}\,\mathrm{cm}^{-2}$ and *intrinsic* luminosities are in units of $10^{41}\,\mathrm{erg\,s}^{-1}$ (for an assumed distance of 56 Mpc).

Model	N_{H}	kT	N_{H}	kT	N_{H}	kT or Γ	χ^2_{red}(dof)	F_{x}	L_{X}
M + M + PL	Gal	$0.50^{+0.12}_{-0.17}$	$3.7^{+0.5}_{-0.7}$	$0.88^{+0.21}_{-0.14}$	†	$2.42^{+0.17}_{-0.21}$	1.16(80)	11.72	7.67
M + M + PL§	Gal	$0.58^{+0.05}_{-0.14}$	$7.8^{+1.7}_{-2.1}$	$0.92^{+0.12}_{-0.17}$	$3.4^{+1.3}_{-1.8}$	$1.99^{+0.32}_{-0.36}$	1.07(79)	12.09	9.09

† Same hydrogen column as applied to previous spectral component.
§ Model component normalizations: 1.3×10^{-4} and 5.8×10^{-4} for the 0.6 and 0.9-keV Mekal components, respectively, in units of $(10^{-14}/4\pi D)\times\int n_{\mathrm{e}}^2\,\mathrm{d}V$ (where D is the distance to NGC 3256 in cm, n_{e} is the electron density in cm^{-3}, and V is the volume of the emitting region in cm^3); 1.8×10^{-4} for the power law, in units of 10^{-4} photons $\mathrm{cm}^{-2}\,\mathrm{s}^{-1}\,\mathrm{keV}^{-1}$.

Downloaded from http://mnras.oxfordjournals.org/ at University of Durham on August 8, 2014

consequence of the continuum being largely suppressed. We have examined the *Chandra* data around the position of the southern nucleus and found *no* counts in the 6- to 7-keV energy band, making the scattering scenario unlikely. Finally, recent high-resolution *N*-band observations of NGC 3256 (Lira & Ward 2002) show a weak source ($\sim$50 mJy) coincident with the southern nucleus. Its low luminosity is a strong argument against reprocessing and the presence of a dust enshrouded AGN.

6.1.3 *A low luminosity AGN?*

The presence of a low-luminosity AGN (LLAGN) similar to the one observed in NGC 3031 ($L_X \sim 2 \times 10^{40}$ erg s^{-1} in the 2–10 keV band, Ishisaki et al. 1996) is still plausible, although this possibility would not have a significant impact on the overall energy output of the galaxy. The derived luminosity for the southern nucleus lies at the lower end of the range of luminosities determined by Ptak et al. (1999) for a sample of LLAGNs and LINERs, and somewhat larger than the absorption-corrected luminosity that Iwasawa et al. (2000) determined for the dwarf Seyfert 1 nucleus in NGC 4395.

To address this scenario, we have plotted the extinction-corrected emission from the nuclei of NGC 3256 along with the spectral energy distributions (SEDs) of classical radio-loud and radio-quiet quasars (from Elvis et al. 1994), LLAGN (adapted from Ho 1999) and starburst nuclei (from Schmitt et al. 1997) – see Fig. 9. All the SEDs have been normalized to the observed nuclear flux in the *L*-band. The nuclear data correspond to radio observations published by Norris & Forbes (1995), JHKL observations reported by Kotilainen et al. (1996), HK *NICMOS* observations reported in this paper and *N*-band observations by Lira & Ward (2002). Fig. 9 shows that both nuclei are too X-ray weak to be AGNs, while the radio emission has an intermediate value between the radio-loud AGN and LLAGN, and the radio-quiet AGN. The southern nucleus, however, shows a flat distribution between 1 and 10μm in νF_ν space, which is characteristic of AGNs. Given the large uncertainties in the determination of the X-ray luminosity for this nucleus, the presence of an LLAGN is certainly possible. The northern nucleus, on the other hand, presents a sharp rise towards longer wavelengths, in good agreement with the spectral distribution for starburst galaxies.

For a brief discussion of the possibility that inverse Compton scattering plays a significant role in the X-ray emission from the nuclei, see Section 6.3.4.

6.2 The discrete-source population

We have used archival *HST* observations of NGC 3256 in order to search for optical counterparts of the X-ray sources seen in Fig. 1. The galaxy was imaged with the WFPC2 camera on board *HST* on 1994 May 20 and 1994 September 6, using the F450W ($\sim B$) and F814W ($\sim I$) broad-band filters. The data have already been reported by Zepf et al. (1999).

Fig. 10 shows 0.3–10 keV X-ray iso-contours overlaid onto the *HST* F814W observations and an F450W–F814W colour map. The *Chandra* data have been smoothed using an adaptive smoothing technique developed by Ebeling, White & Rangarajan (1999) and implemented in the CIAO software. The algorithm uses a circular Gaussian with variable width which is adjusted in order to preserve the signal-to-noise ratio under the kernel.

Several coincidences between X-ray sources and optical knots of emission can be seen in Fig. 10. In the nuclear region tentative counterparts can be found for most of the X-ray sources, and in particular for sources 5, 7(N), 9, 10 and 11, which correspond to moderately-absorbed sources, as can be seen in Table 3. On the other hand, those sources with significantly large values of $N_{\rm H}$ (sources 2, 3 and 8) have no clear optical counterparts. The location of these absorbed sources in the F450W–F814W colour image shows a clear correlation between large X-ray hydrogen columns and the presence of prominent dust lanes.

Photometric measurements for the optical counterparts to the less obscured X-ray sources show that they are all characterized by blue colours, with F450W–F814W ~ -0.7 to -1.4 mag. Using the Space Telescope Data Analysis System (STSDAS) Synphot task we have also computed the F450W–F814W colour of the Orion star-forming nebula and found that it is necessary to introduce a visual extinction of ~ 2.5 mag to its spectral energy distribution in order to reproduce the range of colours of the star-forming regions in NGC 3256. From the study of the colour–colour diagram presented in Section 3.2, we have derived typical absorption columns towards these sources of a few times 10^{21} cm^{-2}. Assuming a Galactic gas-to-dust ratio this absorption corresponds to a visual extinction of ~ 1–3 mag.

Lípari et al. (2000) have obtained optical spectra for several sources in the nuclear region of NGC 3256. Their Region 1 corresponds to the northern nucleus, while Regions 2, 4, 5, 8 and 9 are probably the counterparts of the X-ray sources 10, 11, 13, 9 and 6, respectively (from comparison of their fig. 1c with our Hα maps discussed in Section 6.3.1). They found that all spectra are typical of high-metallicity H II regions or starbursts with an extinction of $A_V \gtrsim 2$, in good agreement with our results from the *Chandra* observations and the *HST* photometry.

We have found a clear correlation between powerful and compact X-ray sources and regions of vigorous star formation. A few of the sources are clearly resolved in the *Chandra* data and probably correspond to complex regions of multiple individual sources and diffuse emission similar to a scaled-down version of the nuclear region of M82.

Most of the discrete sources seen in the *Chandra* data are unresolved. The *Chandra* spatial resolution (FWHM $\sim$ 0.5 arcsec) implies that these point-like sources have linear sizes of $\lesssim 140$ pc, only a factor of two smaller than the complex X-ray-emitting region seen in 30 Dor, the giant H II nebula in the LMC (Wang 1999). Therefore, groupings of less-luminous objects contributing to many of these unresolved sources is likely.

Recent work by Helfand & Moran (2001) shows that the hard emission in NGC 3256 can be explained if luminous high-mass X-ray binaries, like those observed in the Magellanic Clouds, are representative of the source population. The 2–10 keV X-ray luminosity from all high-mass X-ray binaries in the LMC or SMC is however, only $\sim 3.5 \times 10^{38}$ erg s^{-1} (Helfand & Moran 2001), at least one order of magnitude below the average luminosity of the point sources seen in NGC 3256 (for $\Gamma = 2$, approximately half the unabsorbed luminosity will emerge in the 2–10 keV energy range – see Table 3). This implies that at least 10, and up to 30, high-mass X-ray binaries ($L_X \gtrsim \times 10^{38}$ erg s^{-1}) need to be clustered in a region half the size of 30 Dor. This might suggest the presence of intrinsically luminous X-ray sources in some of the discrete sources observed in NGC 3256, which would dominate their X-ray output, as is observed, for example, in the M82 starburst galaxy (Griffiths et al. 2000, Kaaret et al. 2001; Ward et al., in preparation).

Downloaded from http://mnras.oxfordjournals.org/ at University of Durham on August 8, 2014

The presence of these point-like and highly-luminous sources in selected nearby galaxies has been recognized for at least a decade (Fabbiano 1989), although only recently has the full scope of this phenomenon emerged from detailed galaxy surveys using high-resolution X-ray observations (Roberts & Warwick 2000; Lira, Lawrence & Johnson, 2000; Colbert & Mushotzky 1999). The nature of these so-called Super Eddington sources (with L_X well above the Eddington limit for a $\sim 1\,M_\odot$ accreting neutron star) is still poorly understood. Candidates to explain them include young supernova remnants evolving in highly-dense environments, accretion onto intermediate-mass black holes, mildly-beamed (but otherwise normal) X-ray binaries, 'hypernova remnants' (i.e. the

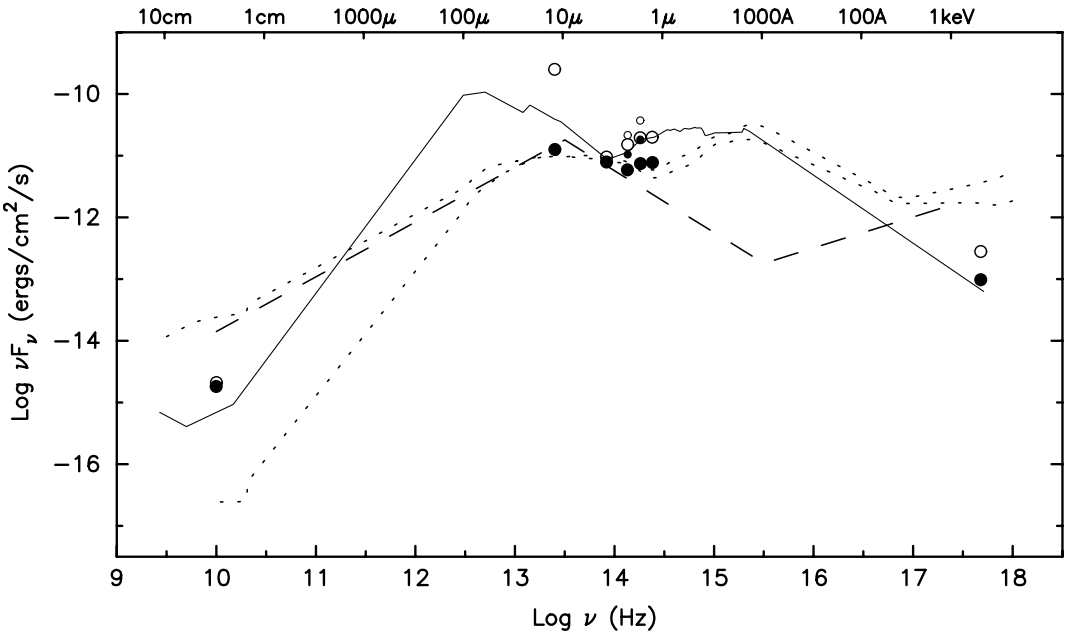

Figure 9. Absorption-corrected fluxes for the northern nucleus (open circles) and southern nucleus (filled circles). Radio and infrared data from Norris & Forbes (1995), Lira & Ward (2002), and Kotilainen et al. (1996); X-ray data from this paper. *NICMOS* HK observations (this paper) are shown with smaller-size symbols. The data are compared with the spectral energy distributions of radio-loud and radio-quiet classical quasars (dotted lines), low-luminosity AGNs (dashed line) and starburst galaxies (solid line). All distributions have been normalized to the nuclear fluxes in the *L*-band (3.5 μm).

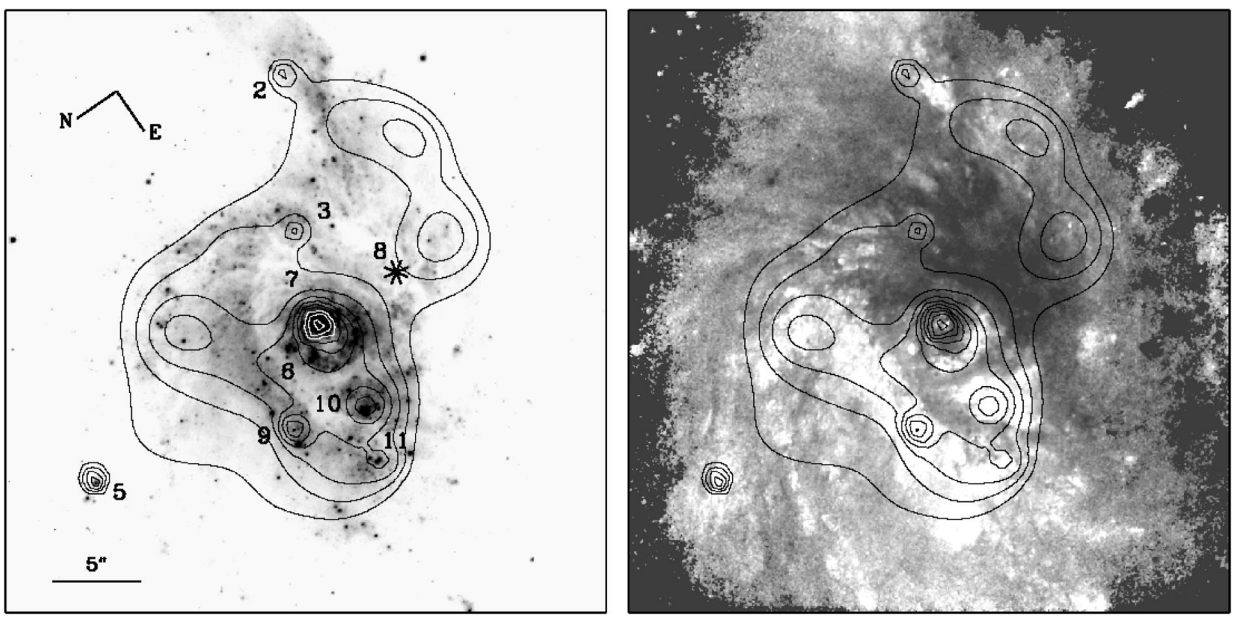

Figure 10. X-ray isocontours overlaid onto optical *HST* PC2 images of the central region in NGC 3256. A broad-band F814W ($\sim I$) image is shown in the left panel and a colour F450W-F814W ($\sim B - I$) image is shown at the right (darker corresponds to redder colours – for a colour version see fig. 2 in Zepf et al. 1999). Both images have the same size and (non-standard) orientation. Compact sources are labelled and the position of the southern nucleus is marked with an asterisk in the top image.

Downloaded from http://mnras.oxfordjournals.org/ at University of Durham on August 8, 2014

remnants of a gamma-ray burst), and compact complexes of several less-luminous X-ray sources. It is quite possible that the Super Eddington sources cannot be grouped into a single type of object but represent a heterogeneous class.

Chandra observations of the archetypal starburst galaxy M82 have revealed a highly-variable and extremely-luminous source ($1-10\times10^{40}\,\mathrm{erg\,s^{-1}}$), which could imply the presence of a $\gtrsim$500-$M_{\odot}$ compact accreting object (Kaaret et al. 2001). Similar massive accreting black holes could explain some of the Super Eddington sources found in NGC 3256. Unfortunately, the lack of significant time variability in the compact-source light curves (Fig. 5) means that we cannot constrain the luminosity of individual sources. However, no very-short-time-scale variability has been detected in the luminous source in M82 suggesting that the dramatic changes in flux are not flares of short duration (Kaaret et al. 2001; Ward et al., in preparation). The same situation is found for the Super Eddington sources detected in the Antennae galaxy (Zezas et al. 2001).

The distribution of luminosities of the NGC 3256 point-source population is presented as a histogram in Fig. 11 (i.e. after discarding the extended sources 2, 9, 10 and both nuclei). We have used a power-law model with $\Gamma = 2$ and corrected the luminosities for Galactic absorption only. Data from *Chandra* observations of the Antennae galaxy have also been included (Zezas et al., in preparation; Fabbiano et al. 2001). The Antennae is the nearest example of a major merger and shows signatures of powerful star-formation activity in both nuclei and throughout the colliding discs. The emission from the galaxy is dominated by the starbursts, although they are not as powerful as that in NGC 3256 (see Table 8).

About 40 point sources have been detected in the Antennae and their observed luminosity distribution is plotted with a thin dotted line in Fig. 11 (extended sources and the nuclei have been excluded; luminosities have been corrected for Galactic foreground absorption). The observations of this system have a much higher sensitivity threshold than the observations of NGC 3256 and the population of point sources has been detected down to luminosities below $\sim 10^{38}\,\mathrm{erg\,s^{-1}}$. The central regions of this merger are affected by significant reddening (Mengel et al. 2001) and the distribution of intrinsic absorbing columns affecting the sources seen in the Antennae is similar to that found for NGC 3256 (Zezas et al., in preparation), making the comparison between these galaxies clearly appropriate.

The distance to the Antennae is 29 Mpc – about half the distance to NGC 3256 – and so the different physical sizes of the X-ray-emitting regions probed in both galaxies can introduce significant differences in the inferred luminosity distribution of the source population. Hence, to perform a meaningful comparison of the sources seen in both galaxies we have degraded the resolution of the *Chandra* observations of the Antennae to that of NGC 3256 and determined the population of point sources. The results are plotted in Fig. 11 with a thick dash–dotted line. Only 30 point sources are found with luminosities between $\sim 10^{38}-10^{40}\,\mathrm{erg\,s^{-1}}$.

The luminosity distribution of sources in both the Antennae and NGC 3256 show a handful of objects with luminosities above $\sim 5\times10^{39}\,\mathrm{erg\,s^{-1}}$. There is, however, a clear deficiency of sources in NGC 3256 below that luminosity, mostly, and perhaps entirely, due to the lower sensitivity of the observations. Comparing the unbinned and binned data for the Antennae, the most significant change is found for sources below $\sim 10^{39}\,\mathrm{erg\,s^{-1}}$. This is mainly due to objects in the lower-resolution data merging with other point sources or the diffuse background to give areas of extended emission. The high-luminosity end, on the other hand, is little changed. If higher spatial resolution was available, some of these sources would probably be found to be multiple lower-luminosity objects, as *Chandra* observations of nearby starburst galaxies like M82 and NGC 253 have shown (Ward et al., in preparation; Strickland et al. 2000). Nevertheless, the existence of Super Eddington sources remains a strong possibility for both NGC 3256 and the Antennae.

6.3 The origin of the X-ray emission

6.3.1 Correlation with Hα emission

In order to investigate the morphology of the diffuse component in NGC 3256 further, we subtracted circular regions with a radius of 3 arcsec (which encircles $\sim$ 90 per cent of the incident photons) on a full band (0.3–10 keV) image of the galaxy at the positions of the detected discrete sources to remove their emission. We then interpolated over the holes and smoothed the image with a Gaussian with $\sigma = 1$ arcsec, obtaining a diffuse component map. Subtracting this frame of the diffuse emission from the original image we obtained an image of the population of compact sources only. This compact-source map was then slightly smoothed ($\sigma = 1$ arcsec).

The two X-ray images were then compared with an archive Hα observation of the galaxy obtained with the New Technology Telescope at La Silla in April 1993. The Hα and associated calibration frames were reduced in the standard manner. The final Hα image was obtained by scaling the 'line' and 'continuum' images until a good subtraction of the field stars was achieved.

Fig. 12 shows the X-ray contours of the diffuse- and discrete-source population overlaid onto the Hα image of NGC 3256 (the 'roundness' of the contours representing each compact source is an artefact resulting from the smoothing of the image using a Gaussian profile). In general, there is good agreement between the morphology seen in both wavebands. The most prominent regions seen in Hα are nearly always coincident with enhanced regions of diffuse X-ray emission. Also, several X-ray compact sources are coincident with strong Hα knots. One interesting feature corresponds to the Hα emission coincident with source 10, where a bubble-like morphology can be seen. On the other hand, no strong Hα emission is detected at the position of the southern 'Arm' seen in diffuse X-rays. Also, none of the compact sources located in this region (sources 2, 3 and 8) have obvious counterparts in the Hα image. As mentioned in Section 6.1, *H*, *K* and Paα observations of NGC 3256 were obtained with *NICMOS*. The small field of view of the NIC2 camera was centred around the most obscured part of the galaxy and contained sources 7, 8, 2 and 3. Again, no counterparts were found for sources 2 and 3 in any of the *NICMOS* images, ruling out a direct association with powerful HII regions or a young dusty stellar cluster.

A crude flux calibration of the Hα image can be achieved using the long slit observations reported by Lípari et al. (2000). They obtained Hα fluxes for the brightest knots of emission within the central region of the galaxy through a slit width of 1.5–2.0 arcsecs. Inspection of the Hα image shows that these apertures contain the bulk of the emission for those knots used in the calibration. The spectrophotometric fluxes were compared with the background-subtracted counts obtained from the Hα image using a 2 arcsec circular aperture, giving consistent flux-to-count ratios within a factor of two. Using a large circular aperture ($\sim$41 arcsec in diameter) we find that the total Hα flux detected in the NTT image

Downloaded from http://mnras.oxfordjournals.org/ at University of Durham on August 8, 2014

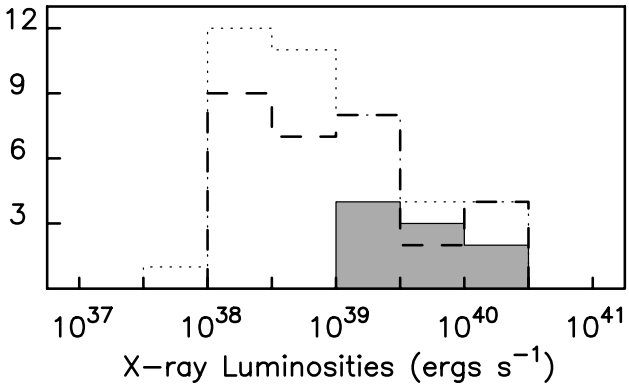

Figure 11. Luminosity distribution of the point-source population in NGC 3256 (shaded area) compared with the observed (thin dotted line) and binned (thick dashed line) population seen in the Antennae galaxy (Fabbiano, Zezas & Murray et al. 2001). See text for details.

Table 8. Properties of the starbursts in NGC 3256 and the Antennae galaxy. References: (1) Hummel & van der Hulst 1986, (2) Stanford et al. 1990, (3) Neff & Ulvestad 2000, (4) Norris & Forbes 1995, (5) Heckman, Armus & Miley 1990. Infrared luminosities were obtained using *IRAS* fluxes (e.g. Helou et al. 1988) and a distance to the Antennae of 29 Mpc.

	L_{6cm} (erg s^{-1})	L_{IR} ($L_\odot$)	SFR ($M_\odot\,yr^{-1}$)	Refs
Antennae	$\sim 1\times10^{39}$	$\sim 6\times10^{10}$	5–6	1, 2, 3
NGC 3256	$\sim 5\times10^{39}$	$\sim 6\times10^{11}$	40–80	4, 5

corresponds to $\sim 2\times10^{-11}$ erg s^{-1} cm^{-2}, or $\sim 7.5\times10^{42}$ erg s^{-1}. The Hα luminosity is therefore $\sim$300 times less than the infrared luminosity of the galaxy. Moorwood & Oliva (1994) estimated that $L_{IR}/H_\alpha \sim 175$ after correcting for absorption, and showed that this value agrees well with models of star formation in galaxies.

The Hα morphology, particularly in the less reddened regions of the galaxy, is a good indicator of the most active star-forming regions. In particular the good agreement seen between several compact sources detected both in X-rays and Hα is a good indicator of the presence of young supernova remnants or rich associations of massive OB stars, and therefore high-mass X-ray binaries.

6.3.2 *The thermal components*

At least two thermal components are necessary to fit the *Chandra* spectrum of the diffuse emission in NGC 3256. The thermal energy associated with a thermal plasma can be expressed as $E_x = 3n_e VfkT$. The electron density, n_e, can be derived from the emission integral (EI), which is given by the component normalization during the fit to the X-ray data. Assuming a purely ionized hydrogen gas, $EIfn_e^2V$, where f is the filling factor, or fraction of the volume V occupied by the X-ray-emitting gas. If this emission is indeed powered by the starburst activity in the galaxy then E_x should be no larger than the amount of energy that the starburst has injected into the interstellar medium. This comparison assumes that the injected mass and energy, in the form of stellar winds and SN ejecta, has been efficiently thermalized to a characteristic temperature T, and evolved into a galactic wind.

MLH have already shown that the thermal energy stored in the X-ray-emitting gas in NGC 3256 is consistent with the amount of energy injected by the starburst in the last $\sim 10^7$ yr ($\sim$ few 10^{57} erg). The spectral parameters derived from our *Chandra* observations for the two thermal components are different from those derived from the *ASCA* data (in terms of best-fit temperatures and normalizations – see last entry in Table 4), but these differences would only amount to an increase of $\sim$30 per cent in our estimate of the total E_x (by considering both the cool and warm components). This relatively small change is due to the opposite effects introduced by the higher temperature we find for the cooler component (0.6 keV instead of the 0.3 keV derived from the *ASCA* data) and the lower normalization we determine for the warm component ($\sim$ 2.7 times smaller than the one derived by MLH). Still, a larger difference could be introduced if different geometries are assumed for the regions occupied by the plasma.

In principle, from the spatially-resolved spectroscopy, we could constrain the characteristic sizes of the regions occupied by the thermal emission, in particular the volume V occupied by the warm component, which was unconstrained by the *ASCA* observations (MLH assumed a spherical geometry with $r = 1.4$ kpc centred on the northern nucleus). Our tentative results show that the 0.6-keV component dominates for $r \gtrsim 4$ kpc whilst the 0.9-keV gas dominates over $r \lesssim 3$ kpc, with an intermediate ~ 0.8 keV temperature found in between. The results are less certain if more realistic errors are computed using two parameters of interest for a 90 per cent CL (i.e. $\Delta\chi^2 = 4.6$) : while region A is characterized by $N_H \sim 0.4$–1.0 cm^{-2} and $T \sim 0.6$–0.9 keV, region B is described by $N_H \sim 0.1$–0.5 cm^{-2} and $T \sim 0.5$– 0.7 keV. As noted in Section 4.2, the result on the N_H variation between the two regions is better constrained than the temperature variation.

Although not well constrained, our results suggest that the characteristic radius adopted by MLH for the spherical region occupied by the warm component could have been underestimated by about a factor two. The larger volume implies that the thermal energy stored in the 0.9-keV plasma could be as high as $\sim 1\times10^{57}$ erg (for a fitted value of $EI = 1.9\times10^{64}$ cm^{-3} and $f = 1$). Also, the *Chandra* data have shown that the cool component extends further than the 6-kpc radius adopted by MLH, especially towards the north-east of the galaxy (see Fig. 8). The energetics in this component will be at most $\sim 1.5\times10^{57}$ erg (for $r = 8$ kpc, a fitted value of $EI = 4.2\times10^{63}$ cm^{-3} and $f = 1$).

The total energy stored in the thermal components is therefore in good agreement with the derived energy deposited by the starburst activity over the last $\sim 10^7$ yr. It should be remembered, however, that not all the kinetic output, in the form of star winds and supernova ejecta, is effectively thermalized in the form of a galactic wind. Although difficult to estimate, numerical simulations predict thermalization efficiencies of $\gtrsim 50$ per cent (Strickland 2001). If this figure is applicable to NGC 3256, then only half of the energy released by the starburst ($\gtrsim 1\times10^{57}$ erg) would be in the form of the hot plasma observed with *Chandra*. However, taking into account that a volume filling factor close to unity for both thermal components is highly unlikely, it is still energetically possible for the starburst to power the observed X-ray emission in NGC 3256.

6.3.3 *The galactic wind*

Although the gross properties of galactic winds are well described by theoretical models, important aspects of the nature of the X-ray emission are not understood. In particular the detailed origin of the X-rays is still an open question. In the scenario proposed by

Downloaded from http://mnras.oxfordjournals.org/ at University of Durham on August 8, 2014

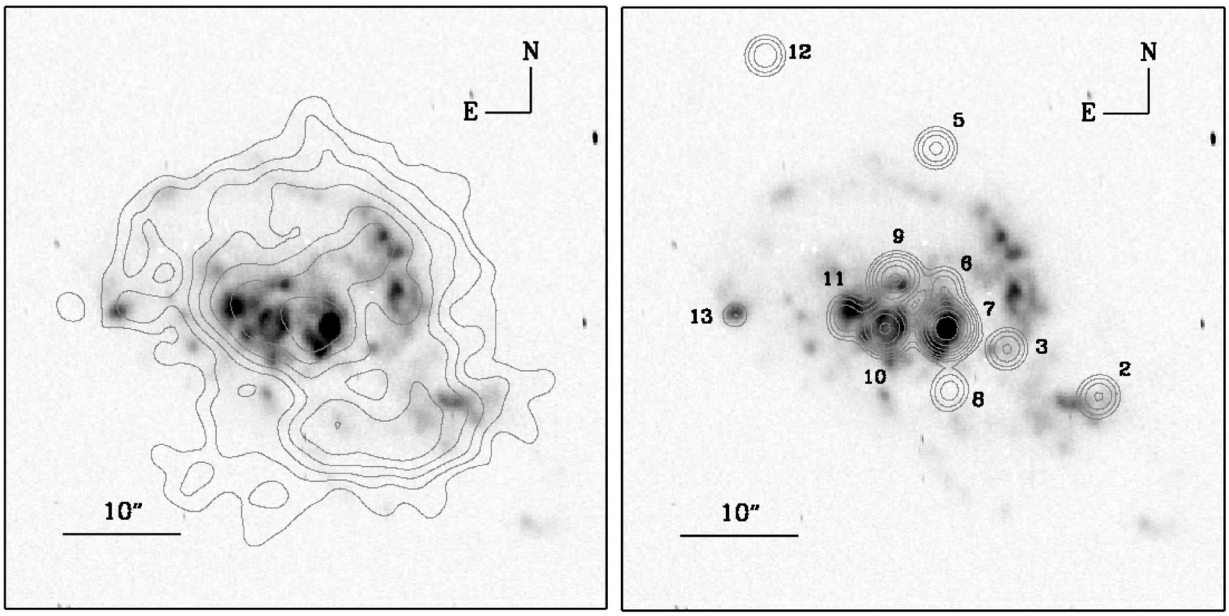

Figure 12. Diffuse (left) and discrete-source population (right) X-ray contours in the 0.3–10 keV energy range overlaid onto an archive Hα image of NGC 3256.

'mass-loading' models, the bulk of the X-rays are produced by a wind that has significantly increased its density and decreased its temperature owing to heavy and efficient mixing with denser interstellar material (see, for example, Suchkov et al. 1996). In this scenario, the physical parameters derived for the X-ray-emitting material correspond to those of the wind itself. Support for the 'mass-loading' scenario in many galaxies comes from the comparison between the mass deposition by the starburst and the X-ray-emitting mass – e.g. M82 and NGC 253 (Ptak et al. 1997), Arp220 (Heckman et al. 1996), NGC 4449 (della Ceca, Griffiths & Heckman 1997) and Arp299 (Heckman et al. 1999). HLM have shown that the wind must also be heavily mass-loaded in NGC 3256. On the other hand, some models postulate that the X-ray emission comes from the interaction of the hot and low-density wind with clouds of gas, either ambient material that has been engulfed within the wind or that is located at the boundary layer between the flow and the surrounding medium (e.g. Chevalier & Clegg 1985). In this case the tenuous wind remains largely undetectable while the X-ray emission is produced by the low-volume-filling-factor gas from the shocked clouds. If this is the case for NGC 3256, the calculations above should use $f \ll 1$ and take into account that a large fraction of the wind remains invisible in our observations. Recent *Chandra* observations of a limb-brightened outflow in NGC 253 are in good agreement with the idea that the X-rays are produced in the regions of interaction between the hot wind and the denser interstellar medium (Strickland et al. 2000). *XMM-Newton* observations, on the other hand, show that at lower energies the emission is more uniformly distributed, implying a higher filling factor and, probably, a 'mass-loaded' wind (Pietsch et al. 2001).

6.3.4 *The temperature gradient*

Finally, our results in Section 4.2 have suggested a gradient of temperature with radius. A similar distribution of temperatures has already been found in a study of the starburst galaxy M82 by Strickland et al. (1997). They determined a temperature profile given by $T \propto z^{-\alpha}$, with z the distance along the minor axis of the galaxy, and $\alpha \sim 0.2$–0.5. Given the poorly constrained temperatures in NGC 3256, only a rough profile can be derived. Adopting a characteristic temperature of 0.9 keV at the projected distance $r \sim 1$ kpc and 0.6 keV at $r \sim 6$ kpc gives a power-law index $\alpha \gtrsim 0.2$. We cannot compare this value with those derived for M82 or with theoretical predictions until we take into account the projection effects, i.e. the superposition of different regions of the flow in our two-dimensional view of the starburst. However, the nearly spherical geometry of the wind coupled with an axis of the outflow almost coincident with the line of sight, as derived from kinematic studies (Lípari et al. 2000), implies that a flux-weighted average of the temperature along the galaxy minor axis returns exactly the same power-law index as the original spherical distribution. Assuming that the intensity of the emission is proportional to the density squared ($I \propto \rho^2$) and that $\rho \propto R^{-\beta}$ and $T \propto R^{-\alpha}$, with R the radial distance from the centre of the starburst in spherical coordinates, it follows that

$$\frac{\int_{z=0}^{\infty} IT\,\mathrm{d}z}{\int_{z=0}^{\infty} I\,\mathrm{d}z} \propto \frac{1/r^{2\beta+\alpha-1}}{1/r^{2\beta-1}} \propto r^{-\alpha}$$

with $R^2 r^2 + z^2$. In the case of M82, which is viewed nearly edge on, Strickland et al. (1997) adopted a cylindrical geometry for the wind but showed that if the flow properties follow a conical or spherical geometry instead then the measured temperature profile will be slightly flatter than the real distribution. Our result for NGC 3256 is within the range of values found for M82 and is much flatter than the prediction of $\alpha = 4/3$ using adiabatic models (Chevalier & Clegg 1985). However, as explained above, the Chevalier & Clegg model postulates that the X-ray emission does not come from the wind itself, but from shocked clouds of gas. The temperature reached by these clouds will depend on the speed of the shock driven into them by the wind. A shock-heated-cloud

Downloaded from http://mnras.oxfordjournals.org/ at University of Durham on August 8, 2014

model is indeed in good agreement with the results obtained for M82 (for further discussion see Strickland et al. 1997).

6.3.5 *The hard emission*

MLH have argued that the 2–10 keV intrinsic luminosity in the power-law component ($\sim 2\times10^{41}$ erg s^{-1} as measured by *ASCA*) could not be explained solely by the presence of a Galactic population of high-mass X-ray binaries and that inverse Compton scattering was likely to make a significant contribution. They reached this conclusion by comparing the hard X-ray luminosity per O star observed in our Galaxy with the one inferred for NGC 3256. New results published by Helfand & Moran (2001) show that in fact the 2–10 keV luminosity is well explained if a Magellanic Cloud type population of high-mass X-ray binaries is assumed instead of a Galactic population.

Chandra observations show that most of the power-law component seen with *ASCA* can be identified with a population of discrete sources. These extremely bright sources can have luminosities at least one order of magnitude above any source seen in our Galaxy. From a comparison of the luminosity in the discrete-source population and the diffuse component in the 2.5–10 keV range we find that $\sim$ 75–80 per cent of the emission ($\sim 1.2\times10^{41}$ erg s^{-1}) comes from the hard ($\Gamma\sim2$) and powerful (10^{39}–10^{40} erg s^{-1}) compact sources resolved by *Chandra*. A few of these sources have been found to be extended and therefore they probably correspond to compact star-forming regions. Since it is becoming increasingly evident that super Eddington sources are often found in galaxies undergoing vigorous episodes of star formation, we can speculate that some of the observed discrete sources found in NGC 3256 correspond to (or are dominated by) these high luminosity sources. It is, however, impossible to test this further with the present data.

The extended emission has a power-law component characterized by a fairly steep slope ($\Gamma\lesssim3$, or $kT\sim4$ keV if a Mekal model is adopted). This component represents $\sim$75 per cent of the total luminosity in the diffuse emission in the 2.5–10 keV band (see Table 5). An image in this energy range would determine the morphology of the $\Gamma\sim3$ emission, but our data do not have sufficient counts for this. From the spectral fit in Table 5, however, we know that a moderate extinction is associated with this component, and therefore it is unlikely that the bulk of the emission is connected with the innermost, and more-heavily-reddened, parts of the starburst. Also, the inclusion of this component in the fit to the different spatial regions seen in Fig. 8 always gave acceptable values of $\chi^2_{\rm red}$, suggesting that the emission is present even at large radii. Therefore, the $\sim 4\times10^{40}$ erg s^{-1} emitted in the 2.5–10 keV range in the power-law component is most likely due to an unresolved population of X-ray binaries and supernova remnants distributed throughout the galactic disc. The inferred temperature is at the top end of the range of temperatures measured for young supernova remnants ($kT\sim1$–4 keV; Bregman & Pildis 1992) and is close to the temperatures observed in low-mass X-ray binaries ($kT\sim3$ keV; Barret 2001). Inclusion of some contribution from the harder spectra of high-mass X-ray binaries and X-ray pulsars would improve the spectral match.

6.3.6 *Inverse Compton scattering?*

Our *Chandra* observations have shown that most of the $\Gamma\lesssim2$ power-law emission is accounted for by hard and powerful discrete sources. So far we have speculated that accretion onto compact objects is the dominant mechanism responsible for this emission. However, inverse Compton (IC) scattering is also a viable non-thermal mechanism that could contribute significantly.

NGC 3256 shows strong infrared and non-thermal (synchrotron) radio emission. This implies the spatial co-existence of a population of relativistic electrons and infrared seed photons that could be up-scattered by the electrons into X-ray frequencies. The IC luminosity can be expressed as $L_{\rm IC}L_{\rm syn}\times U_{\rm ph}U_{\rm B}$, where $L_{\rm syn}$ is the radio luminosity and $U_{\rm ph}$ and $U_{\rm B}$ are the seed photon and magnetic energy densities, respectively (cf. Rybicki & Lightman 1979). The low surface brightness of the radio and infrared emission outside the nuclei implies that IC emission is probably negligible in the extranuclear regions. For example, source 10 in Fig. 1, the brightest source seen outside the nuclei at X-ray and optical wavelengths (for optical broad-band data, see table 3 in Lípari et al. 2000), appears much fainter than the nuclei in the *L*-band map presented by Kotilainen et al. (1996) and in the radio maps by Norris & Forbes (1995), implying a small value for the $L_{\rm syn}\times U_{\rm ph}$ product.

In the case of the nuclei, however, IC emission could still play a significant role in the production of hard X-rays. This is particularly relevant in the case of the northern nucleus, which has a 2–10 luminosity of $\sim 2.5\times10^{40}$ erg s^{-1} (which is completely dominated by the power-law component) and has been found to be an extended source in X-rays (FWHM $\sim$1 arcsec). A similar size has also been determined from radio and *N*-band (12-μm) observations (Norris & Forbes 1995; Lira & Ward 2002), although a much smaller peak is determined from *NICMOS* data at 2.2μm (Section 6.1.1). MLH have shown that between 5×10^{39} and 5×10^{40} erg s^{-1} could be produced by IC scattering in each nucleus in the 2–10 keV band.

If IC scattering does take place, the power-law spectra of the radio and X-ray emission are expected to have the same slope, since the index of the power-law distribution of the electron energies (n) determines the output spectrum for synchrotron and IC radiation in the same manner – $\alpha=(n-1)/2$, where α is the power-law energy index of the out-coming spectra. From the radio observations of NGC 3256 (Norris & Forbes 1995) we find that the power-law index of the radio emission in the nuclei has $\alpha\sim0.8$. This value is inconsistent with the X-ray index observed in the northern nucleus power law ($\alpha=\Gamma-1\sim1.2$–2.4 – see Table 2). More realistic errors, with three parameters of interest for a 90 per cent CL (i.e. $\Delta\chi^2=6.3$) imply that $\alpha\sim1$–2.8, with a lower limit closer to the value of the radio index. No detailed comparison can be made for the southern nucleus, although the (poorly constrained) range of power-law indices derived in Section 3.2 is consistent with the observed radio slope. Therefore, IC emission cannot be dismissed as a possibly significant component of the observed hard luminosities from both nuclei, although this emission can also be explained solely by the output from accretion-driven sources, and, in particular, by the presence of super-Eddington sources.

7 CONCLUSIONS AND SUMMARY

Until recently, the detailed study of the diffuse emission and point-source population in starburst galaxies has been a difficult task. The poor spatial resolution and limited wavelength coverage of X-ray missions prior to *Chandra* have resulted in an incomplete picture. *Einstein* and *ROSAT* images were able to detect a diffuse component and resolve some of the point sources in several starburst galaxies, but their narrow spectral energy range gave only

Downloaded from http://mnras.oxfordjournals.org/ at University of Durham on August 8, 2014

partial information on the complex multi-components making up the emission. Satellites with wider spectral coverage (*ASCA, BeppoSAX*), were able to study the X-ray emission of starburst galaxies up to harder energies, but their extremely low spatial resolution gave little or no information about the different spatial components. This situation is now changing dramatically as *Chandra* data for starburst galaxies become available.

In this paper we have presented a detailed spatial and spectral analysis of *Chandra* observations of the infrared-luminous merger system, NGC 3256. Our main results can be summarized as follows.

(1) The total absorption-corrected luminosity of the galaxy over the 0.5–10 keV energy range is $L_X \sim 9 \times 10^{41}$ erg s^{-1} ($\sim$50 per cent of the luminosity inferred from previous *ASCA* observations owing to the different models adopted). A significant fraction ($\sim$80 per cent) of the X-ray emission is detected as diffuse emission. Fourteen compact sources are detected, with absorption-corrected luminosities between $\sim 10^{39}$ and $\sim 10^{41}$ erg s^{-1}. The X-ray spectra of the diffuse emission is predominantly soft, while the discrete sources exhibit characteristically harder spectra.

(2) Both galaxy nuclei are clearly detected in X-rays. The northern nucleus is spatially resolved (FWHM $\gtrsim$ 270 pc) and it corresponds to the brightest source, with a corrected luminosity of $\sim 1 \times 10^{41}$ erg s^{-1} in the 0.5–10 keV range. The southern nucleus is a heavily obscured source and with an intrinsic luminosity ~ 3–4×10^{40} erg s^{-1}. No clear evidence is found for the presence of an AGN in the southern nucleus.

(3) All the detected discrete sources have luminosities one order of magnitude above the Eddington limit for a $\sim$1-M$_\odot$ accreting neutron star. No doubt fainter point sources are present but are below the sensitivity threshold of our observations. No variability was detected in any of the sources found in NGC 3256, and we were therefore unable to constrain the luminosity of *individual* sources. However, intrinsically powerful sources ($L_X \gtrsim 10^{39}$ erg s^{-1}) are very likely to be present.

(4) The diffuse emission has a soft spectrum that can be described as the superposition of two thermal-plasma components with temperatures $T \sim 0.6$, 0.9 keV plus a harder tail with $\Gamma \sim 3$. Tentative evidence is found from spatially-resolved spectra for a trend in the extinction and the temperature of the thermal plasma to decrease with larger radial distances from the nuclear region, in agreement with observations of other starburst galaxies and with wind models.

(5) The morphology of the diffuse emission and the location of the discrete sources show a good correlation with optical and Hα images. The extinction determined from the X-rays is in good agreement with the values derived from optical and infrared *NICMOS* data.

(6) While the thermal components in the diffuse emission can be explained in terms of the mass and energy deposition by the nuclear starburst, the observed hard tail is best explained by a combination of a population of faint point sources and hot plasma emission from young SNRs. Inverse Compton scattering could still be important in explaining the hard X-rays seen in the two nuclei.

ACKNOWLEDGMENTS

We thank Pepi Fabbiano for kindly making available results from *Chandra* observations of the Antennae galaxy. The archival data are based on observations made with ESO Telescopes at La Silla under programme ID 51.2-0036 and on observations made with the NASA/ESA *Hubble Space Telescope*, obtained from the data archive at the Space Telescope Institute. STScI is operated by the association of Universities for Research in Astronomy, Inc. under the NASA Contract NAS 5-26555. This work was supported by CXC Grant GO1-2116X. AZ acknowledges support by NASA Contract NAS8-39073 (CXC). Data were reduced using Starlink facilities.

REFERENCES

Alonso-Herrero A., Rieke M. J., Rieke G. H., Scoville N. Z., 2000, ApJ, 532, 845
Awaki H., Ueno S., Koyama K., Tsuru T., Iwasawa K., 1996, PASJ, 48, 409
Barret D., 2001, AdSpR, in press, (preprint astro-ph/0101295)
Bregman J. N., Pildis R. A., 1992, ApJ, 398, L107
Cardelli J. A., Clayton G. C., Mathis J. S., 1989, ApJ, 345, 245
Chevalier R. A., Clegg A. W., 1985, Nat, 317, 44
Colbert E. J. M., Mushotzky R. F., 1999, ApJ, 519, 89
della Ceca R., Griffiths R. E., Heckman T. M., 1997, ApJ, 485, 581
Doyon R., Joseph R. D., Wright G. S., 1994, ApJ, 421, 101
Ebeling H., White D. A., Rangarajan F. V. N., 1999, MNRAS, accepted
Elvis M. et al., 1994, ApJSS, 95, 1
Fabbiano G., 1989, ARA&A, 87, 27
Fabbiano G., Zezas A., Murray S. S., 2001, ApJ, 554, 1035
Gehrels N., 1986, ApJ, 303, 336
Genzel R. et al., 1998, ApJ, 498, 579
George I. M., Turner T. J., Netzer H., Nandra K., Mushotzky R. F., Yaqoob T., 1998, ApJSS, 114, 73
Glass I. S., Moorwood A. F. M., 1985, MNRAS, 214, 429
Graham J. R., Wright G. S., Meikle W. P. S., Joseph R. D., Bode M. F., 1984, Nat, 310, 213
Griffiths R. E., Ptak A., Feigelson E. D., Garmire G., Townsley L., Brandt W. N., Sambruna R., Bregman J. N., 2000, Sci, 290, 1325
Heckman T. M., Armus L., Miley G. K., 1990, ApJSS, 74, 833
Heckman T. M., Dahlem M., Eales S. A., Fabbiano G., Weaver K., 1996, ApJ, 457, 616
Heckman T. M., Armus L., Weaver K. A., Wang J., 1999, ApJ, 517, 130
Helfand D. J., Moran E. C., 2001, ApJ, 554, 27
Helou G., Khan I. R., Malek L., Boehmer L., 1988, ApJSS, 68, 151
Ho L. C., 1999, ApJ, 516, 672
Hummel E., van der Hulst J. M., 1986, A&A, 155, 151
Ishisaki et al., 1996
Iwasawa K., Fabian A. C., Almaini O., Lira P., Lawrence A., Hayashida K., Inoue H., 2000, MNRAS, 318, 879
Joseph R. D., Wright G. S., 1985, MNRAS, 214, 87
Kaaret P., Prestwich A. H., Zezas A., Murray S. S., Kim D.-W., Kilgard R. E., Schlegel E. M., Ward M. J., 2001, MNRAS, 321, L29
Kotilainen J. K., Moorwood A. F. M., Ward M. J., Forber D. A., 1996, A&A, 305, 107
Lípari S., Díaz R., Taniguchi Y., Terlevich R., Dottori H., Carranza G., 2000, AJ, 120, 645
Lípari S. et al., 2001, preprint (astro-ph/0007316)
Lira P., Lawrence A., Johnson R. A., 2000, MNRAS, 319, 17
Lutz D., Veilleux S., Genzel R., 1999, ApJL, 517, L13
Maiolino R., Salvati M., Bassani L., Dadina M., della Ceca R., Matt G., Risaliti G., Zamorani G., 1998, A&A, 338, 781
Matt G., Fabian A. C., Guainazzi M., Iwasawa K., Bassani L., Malaguti G., 2000, MNRAS, 318, 173
Mengel S., Lehnert M. D., Thatte N., Tacconi-Garman L. E., Genzel R., 2001, ApJ, 550, 280
Moorwood A. F. M., Oliva E., 1994, ApJ, 429, 602
Moran E. C., Lehnert M. D., Helfand D. J., 1999, ApJ, 526, 649, (MLH)
Mukai K., 1993, Legacy, 3, 21
Neff S. G., Ulvestad J. S., 2000, AJ, 120, 670
Norris R. P., Forbes D. A., 1995, ApJ, 446, 594
Pietsch W., Vogler A., Klein U., Zinnecker H., 2000, A&A, 360, 24
Pietsch W. et al., 2001, A&AL, 365, L174

Downloaded from http://mnras.oxfordjournals.org/ at University of Durham on August 8, 2014

Ptak A., Serlemitsos P., Yaqoob T., Mushotzky R. F., Tsuru T., 1997, AJ, 113, 1286
Ptak A., Serlemitsos P., Yaqoob T., Mushotzky R. F., 1999, ApJSS, 120, 179
Rigopoulou D. et al., 1996, A&A, 315, L125
Roberts T. P., Warwick R. S., 2000, MNRAS, 315, 98
Rybicki G. B., Lightman A. P., 1979, Radiative Processes in Astrophysics. Wiley-Interscience
Sanders D. B., Mirabel I. F., 1996, ARA&A, 34, 749
Sanders D. B., Soifer B. T., Elias J. H., Madore B. F., Matthews K., Neugebauer G., Scoville N. Z., 1988, ApJ, 325, 74
Schmitt H. R., Kinney A. L., Calzetti D., Storchi Bergmann T., 1997, AJ, 114, 592
Stanford S. A., Sargent A. I., Sanders D. B., Scoville N. Z., 1990, ApJ, 349, 492
Strickland D. K., 2001, in Chemical Enrichment of the ICM and IGM. Preprint (astro-ph/0107116)
Strickland D. K., Ponman T. J., Stevens I. R., 1997, A&A, 320, 378
Strickland D. K., Heckman T. M., Weaver K. A., Dahlem M., 2000, AJ, 120, 2965
Suchkov A. A., Berman V. G., Heckman T. M., Balsara D. S., 1996, ApJ, 463, 528
Wang Q. D., 1999, ApJL, 510, L139
White N. E., Nagase F., Parmar A. N., 1995, in Lewin W. H. G., van Paradijs J., van der Heuvel E. P. J., eds, X-ray Binaries. Cambridge Univ. Press, p. 1
Zepf S. E., Ashman K. M., English J., Freeman K. C., Sharples R. M., 1999, AJ, 118, 752
Zezas A., Fabbiano G., Rots A. H., Murray S. S., 2001, ApJ, submitted

This paper has been typeset from a TEX/LATEX file prepared by the author.

Downloaded from http://mnras.oxfordjournals.org/ at University of Durham on August 8, 2014